Multi-body Integrated Vehicle-Occupant Models for Collision Mitigation and Vehicle Safety using Dynamics Control Systems

[a,b,] Mustafa Elkady, [c*]Ahmed Elmarakbi, [c]John MacIntyre and [c]Mohamed Alhariri

[a]Department of Mechanical Engineering, School of Engineering, Lebanese International University (LIU), Mouseitbeh - Beirut - Lebanon

[b]Department of Automotive Engineering, Faculty of Engineering, Ain Shams University, Cairo, Egypt

[c]Department of Computing, Engineering and Technology, University of Sunderland,

The Sir Tom Cowie Campus at St Peter's, St Peter's Way, Sunderland, SR6 0DD, UK

E-mail: ahmed.elmarakbi@sunderland.ac.uk

Fax No: +44 (191) 515 2781

*Corresponding author

ABSTRACT

The aim of this paper is to investigate the effect of vehicle dynamics control systems (VDCS) on both the collision of the vehicle body and the kinematic behaviour of the vehicle's occupant in case of offset frontal vehicle-to-vehicle collision. A unique 6-Degree-of-Freedom (6-DOF) vehicle dynamics/crash mathematical model and a simplified lumped mass occupant model are developed. The first model is used to define the vehicle body crash parameters and it integrates a vehicle dynamics model with a vehicle front-end structure model. The second model aims to predict the effect of VDCS on the kinematics of the occupant. It is shown from the numerical simulations that the vehicle dynamics/crash response and occupant behaviour can be captured and analysed quickly and accurately. Furthermore, it is shown that the VDCS can affect the crash characteristics positively and the occupant behaviour is improved.

Keywords: Vehicle safety; collision mitigation; vehicle dynamics and control; mathematical modelling; occupant kinematics

1. INTRODUCTION

Vehicle dynamics control systems (VDCS) exist on the most modern vehicles and play important roles in vehicle ride, stability, and safety. For example, Anti-lock brake system (ABS) is used to allow the vehicle to follow the desired steering angle while intense braking is applied (Yu et al., 2002). In addition, the ABS helps reducing the stopping distance of a vehicle compared to the conventional braking system. The Active suspension control system (ASC) is used to improve the quality of the vehicle ride and reduce the vertical acceleration (Yue et al., 1988; Alleyne and Hedrick, 1995). From the view of vehicle transportation safety, nowadays, occupant safety becomes one of the most important research areas and the automotive industry increased their efforts to enhance the safety of vehicles. Seat belts, airbags, and advanced driver assistant systems (ADAS) are used to prevent a vehicle crash or mitigate vehicle collision when a crash occurs.

The most well known pre-collision method is the advance driver assistant systems (ADAS). The aim of ADAS is to mitigate and avoid vehicle frontal collisions. The main idea of ADAS is to collect data from the road (i.e. traffic lights, other cars distances and velocities, obstacles, etc.) and transfer this information to the driver, warn the driver in danger situations and aide the driver actively in imminent collision. There are different actions may be taken when these systems detect that the collision is unavoidable. For example, the brake assistant system (BAS) (Tamura et al., 2001) and the collision mitigation brake system (CMBS) (Sugimoto and Sauer, 2005) were used to activate the braking instantly based on the behaviour characteristics of the driver, and relative position from the most dangerous other object for the moment.

Using mathematical models in crash simulation is useful at the first design concept because rapid analysis is required at this stage. In addition, the well-known advantage of

mathematical modelling provides a quick simulation analysis compared with FE models. Vehicle crash structures are designed to be able to absorb the crash energy and control vehicle deformations, therefore simple mathematical models are used to represent the vehicle front structure (Emori, 1968). In this model, the vehicle mass is represented as a lumped mass and the vehicle structure is represented as a spring in a simple model to simulate a frontal and rear-end vehicle collision processes. Also, other analyses and simulations of vehicle-to-barrier impact using a simple mass spring model were established by Kamal (1970) and widely extended by Elmarakbi and Zu (2005, 2007) to include smart-front structures. To achieve enhanced occupant safety, the crash energy management system was explored by Khattab (2010). This study, using a simple lumped-parameter model, discussed the applicability of providing variable energy-absorbing properties as a function of the impact speed.

In terms of the enhancing crash energy absorption and minimizing deformation of the vehicle's structure, a frontal structure consisting of two special longitudinal members was designed (Witteman and Kriens, 1998; Witteman, 1999). This longitudinal member system was divided to two separate systems: the first, called the crushing part, guarantees the desired stable and efficient energy absorption; the other, called the supporting part, guarantees the desired stiffness in the transverse direction. For high crash energy absorption and weight efficiency, new multi-cell profiles were developed (Kim, 2002). Various design aspects of the new multi-cell members were investigated and the optimization was carried out as an exemplary design guide.

The vehicle body pitch and drop at fontal impact is the main reason for the unbelted driver neck and head injury (Chang et al., 2006) . Vehicle pitch and drop are normally experienced at frontal crash tests. They used a finite element (FE) method to investigate the frame

deformation at full frontal impact and discussed the cause and countermeasures design for the issue of vehicle body pitch and drop. It found that the bending down of frame rails caused by the geometry offsets of the frame rails in vertical direction during a crash is the key feature of the pitching of the vehicle body.

The effect of vehicle braking on the crash and the possibility of using vehicle dynamics control systems to reduce the risk of incompatibility and improve the crash performance in frontal vehicle-to-barrier collision were investigated (Hogan and Manning, 2007. They proved that there is a slight improvement of the vehicle deformation once the brakes are applied during the crash. A multi-body vehicle dynamic model using ADAMS software, alongside with a simple crash model was generated in order to study the effects of the implemented control strategy.

Their study showed that the control systems were not able to significantly affect the vehicle dynamics in the offset barrier impact. In addition, it was found that in offset vehicle-to-vehicle rear-end collision, the ABS or direct yaw control (DYC) systems can stabilise the vehicle; however, these control systems affected each other and cannot work together at the same time.

The main aim of this research is to investigate the effect of the VDCS on vehicle collision mitigation, enhance vehicle crash characteristics, and improve occupant biodynamics responses in case of 50% vehicle-to-vehicle offset crash scenario.

2. METHODOLOGY

A vehicle frontal collision can be divided into two main stages, the first one is a primary impact, and the second one is a secondary impact. The primary impact indicates the collision between the front-end structure of the vehicle and an obstacle (another vehicle in this paper).

The secondary impact is the interaction between the occupant and the restraint system and/or the vehicle interior due to vehicle collisions.

2.1. Vehicle Dynamics/Crash Model

In this paper, a 6-degree of freedom (DOF) vehicle dynamics/crash mathematical model, shown in Figure 1, has been developed to optimise the VDCS in impending impact at offset vehicle-to-vehicle crash scenarios for vehicle collision mitigation. The ABS and the ASC systems are co-simulated with a full car vehicle dynamic model and integrated with a front-end structure. It is worthwhile mentioning that vehicle components, which significantly affect the dynamics of a frontal impact, are modelled by lumped masses and nonlinear springs.

In this full-car model, the vehicle body is represented by lumped mass m and it has a translational motion in longitudinal direction (x axis), translational motion on vertical direction (z axis), pitching motion (around y axis), rolling motion (around x axis), and yawing motion in case of offset collision (around z axis at the point of impact). Four spring/damper units are used to represent the conventional vehicle suspension systems. Each unit has a spring stiffness k_S and a damping coefficient c. The subscripts f, r, R and L denote the front, rear, right and left wheels, respectively. The ASC system is co-simulated with the conventional suspension system to add or subtract an active force element u. The ABS is co-simulated with the mathematical model using a simple wheel model. The unsprung masses are not considered in this model and it is assumed that the vehicle moves in a flat-asphalted road, which means that the vertical movement of the tyres and road vertical forces can be neglected.

To represent the front-end structure of the vehicle, four non-linear springs with stiffness k_s are proposed: two springs represent the upper members (rails) and two springs represent lower members of the vehicle frontal structure. The subscript u denotes the upper rails while the

subscript l denotes the lower rails. The bumper of the vehicle is represented by a lumped mass m_b and it has a longitudinal motion in the x direction and rotational motion for the non-impacted side of each bumper.

The general dimensions of the model are shown in Figure 1, where l_f, l_r, l and h represent the longitudinal distance between the vehicle's CG and front wheels, the longitudinal distance between the CG and rear wheels, the wheel base and the high of the CG from the ground, respectively. a is the distance between the centre of the bumper and the right/left frontal springs; b is the distance between the CG and right/left wheels.

The free body diagram of the mathematical model is shown in Figure 2, which represents the different internal and external forces applied on the vehicle body. F_s, F_S, F_b, F_z and $F_{f`}$ are front-end non-linear spring forces, vehicle suspension forces, braking forces, normal forces and friction forces between the tyres and the road due to vehicle yawing, respectively.

2.1.1 Equations of motion of vehicle-to-vehicle crash scenario

The model in the case of offset frontal vehicle-to-barrier is thirteen DOF namely longitudinal and vertical movements, pitching, rolling and yawing motions for each vehicle body, the longitudinal movement of the two bumpers as one part, and the rotational motion for the non-impacted side of each bumper. The two bumpers of each vehicle are considered as lumped masses, and dealt as one mass to transfer the load from one vehicle to another. Figures 3 (a) and 3 (b) show the vehicle model before and after collision in case of offset frontal vehicle-to-vehicle crash scenario. The equations of motion of the mathematical model shown in Figure 3 are developed to study and predict the dynamic response of the primary impact of offset vehicle-to-vehicle crash scenario. Figures 4 and 5 are used to describe the deformation of the front springs due to vehicle pitching around its CG and vehicle yawing around the point of impact for the two vehicles, respectively. Figures 1 and 2 are also used to derive the

equations of motion of the two vehicle models. The detailed equations of motion are presented as follows:

$$m_a \cdot \ddot{x}_a + (F_{suRa} + F_{slRa}) \cdot \cos\gamma_a + (F_{suLa} + F_{slLa}) \cdot \cos\phi_a$$

$$+ F_{bfRa} + F_{bfLa} + F_{brRa} + F_{brLa} = 0 \quad (1)$$

$$m_b \cdot \ddot{x}_b + (F_{suRb} + F_{slRb}) \cdot \cos\gamma_b + (F_{suLb} + F_{slLb}) \cdot \cos\phi_b$$

$$+ F_{bfRb} + F_{bfLb} + F_{brRb} + F_{brLb} = 0 \quad (2)$$

$$m_a \cdot \ddot{z}_a + F_{SfRa} + F_{SfLa} + F_{SrRa} + F_{SrLa} = 0 \quad (3)$$

$$m_b \cdot \ddot{z}_b + F_{SfRb} + F_{SfLb} + F_{SrRb} + F_{SrLb} = 0 \quad (4)$$

$$I_{yya} \cdot \ddot{\theta}_a - (F_{SfRa} + F_{SfLa}) \cdot l_{fa} + (F_{SrRa} + F_{SrLa}) \cdot l_{ra}$$

$$+ (F_{suRa} \cdot \cos\gamma_a + F_{suLa} \cdot \cos\phi_a) \cdot d_{1a} - (F_{slRa} \cdot \cos\gamma_a + F_{slLa} \cdot \cos\phi_a) \cdot d_{2a}$$

$$- (F_{bfRa} + F_{bfLa} + F_{brRa} + F_{brLa}) \cdot (z_a + h_a) = 0 \quad (5)$$

$$I_{yyb} \cdot \ddot{\theta}_b - (F_{SfRb} + F_{SfLb}) \cdot l_{fb} + (F_{SrRb} + F_{SrLb}) \cdot l_{rb}$$

$$+ (F_{suRb} \cdot \cos\gamma_b + F_{suLb} \cdot \cos\phi_b) \cdot d_{1b} - (F_{slRb} \cdot \cos\gamma_b + F_{slLb} \cdot \cos\phi_b) \cdot d_{2b}$$

$$- (F_{bfRb} + F_{bfLb} + F_{brRb} + F_{brLb}) \cdot (z_b + h_b) = 0 \quad (6)$$

$$I_{zza} \cdot \ddot{\phi}_a + (F_{suRa} + F_{slRa}) \cdot \cos\gamma_{1a} \cdot a_{oa} - (F_{suLa} + F_{slLa}) \cdot a_{ia}$$

$$- (F_{suRa} + F_{slRa}) \cdot \sin\gamma_{1a} \cdot (l_{aa} - x_a) + (F_{bfRa} + F_{brRa}) \cdot b_{oa} - (F_{bfLa} + F_{brLa}) \cdot b_{ia}$$

$$+ (F_{ffRa} + F_{ffLa}) \cdot (l_{ba} - x_a) + (F_{frRa} + F_{frLa}) \cdot (l_a + l_{ba} - x_a) = 0 \quad (7)$$

$$I_{zzb}\cdot\ddot{\phi}_b+(F_{suRb}+F_{slRb})\cdot\cos\gamma_{1b}\cdot a_{ob}-(F_{suLb}+F_{slLb})\cdot a_{ib}$$

$$-(F_{suRb}+F_{slRb})\cdot\sin\gamma_{1b}\cdot(l_{ab}-x_b)+(F_{bfRb}+F_{brRb})\cdot b_{ob}-(F_{bfLb}+F_{brLb})\cdot b_{ib}$$

$$+(F_{ffRb}+F_{ffLb})\cdot(l_{bb}-x_b)+(F_{ffRb}+F_{ffLb})\cdot(l_b+l_{bb}-x_b)=0 \quad (8)$$

$$I_{xxa}\cdot\ddot{\psi}_a+(F_{SfLa}+F_{SrLa})\cdot b_{ia}-(F_{SfRa}+F_{SrRa})\cdot b_{oa}$$

$$-(F_{ffRa}+F_{ffLa}+F_{ffRa}+F_{ffLa})\cdot(z_a+h_a)$$

$$-F_{suRa}\sin\gamma_{1a}\cdot e_{1a}+F_{slRa}\sin\gamma_{1a}\cdot e_{2a}=0 \quad (9)$$

$$I_{xxb}\cdot\ddot{\psi}_b+(F_{SfLb}+F_{SrLb})\cdot b_{ib}-(F_{SfRb}+F_{SrRb})\cdot b_{ob}$$

$$-(F_{ffRb}+F_{ffLb}+F_{ffRb}+F_{ffLb})\cdot(z_b+h_b)$$

$$-F_{suRb}\sin\gamma_{1b}\cdot e_{1b}+F_{slRb}\sin\gamma_{1b}\cdot e_{2b}=0 \quad (10)$$

$$I_{zzba}\cdot\ddot{\phi}_{ba}-(F_{suRa}+F_{slRa})\cos\gamma_a\cdot l_{oa}\cos\phi_{ba}$$

$$-(F_{suRa}+F_{slRa})\sin\gamma_a\cdot l_{oa}\sin\phi_{ba}=0 \quad (11)$$

$$I_{zzbb}\cdot\ddot{\phi}_{bb}-(F_{suRb}+F_{slRb})\cos\gamma_b\cdot l_{ob}\cos\phi_{bb}$$

$$-(F_{suRb}+F_{slRb})\sin\gamma_b\cdot l_{ob}\sin\phi_{bb}=0 \quad (12)$$

$$m_c\cdot\ddot{x}_c+(F_{suRb}+F_{slRb})\cdot\cos\gamma_b+(F_{suLb}+F_{slLb})\cdot\cos\phi_b$$

$$-(F_{suRa}+F_{slRa})\cdot\cos\gamma_a-(F_{suLa}+F_{slLa})\cdot\cos\phi_a=0 \quad (13)$$

where subscript a denotes vehicle (a) which is equipped with the VDCS and a subscript b denotes vehicle (b) which is used in a free rolling case for all crash scenarios. It is assumed that the two vehicle bumpers are moved in the longitudinal direction of the x axis as one part

and subscript c denotes the equivalent of the two bumpers. d_1 and d_2 represent the distance between the CG and the upper springs force and the lower springs force for each vehicle, respectively and can be calculated using Figure 4 as

$$d_{1a} = \sqrt{l_{fa}^2 + e_{1a}^2} \cdot \sin(\tan^{-1}(\frac{e_{1a}}{l_{fa}}) - \theta_a) \tag{14}$$

$$d_{1b} = \sqrt{l_{fb}^2 + e_{1b}^2} \cdot \sin(\tan^{-1}(\frac{e_{1b}}{l_{fb}}) - \theta_b) \tag{15}$$

$$d_{2a} = \sqrt{l_{fa}^2 + e_{2a}^2} \cdot \sin(\tan^{-1}(\frac{e_{2a}}{l_{fa}}) + \theta_a) \tag{16}$$

$$d_{2b} = \sqrt{l_{fb}^2 + e_{2b}^2} \cdot \sin(\tan^{-1}(\frac{e_{2b}}{l_{fb}}) + \theta_b) \tag{17}$$

where angles γ and γ_1 for each vehicle can also be calculated using Figure 5 as

$$\gamma_a = \tan^{-1}(\frac{l_{oa} - l_{oa}\cos\phi_{ba}}{l_{oa} \cdot \sin\phi_{ba} + l_{\phi Ra} \cdot \cos\phi_a}) \tag{18}$$

$$\gamma_b = \tan^{-1}(\frac{l_{ob} - l_{ob}\cos\phi_{bb}}{l_{ob} \cdot \sin\phi_{bb} + l_{\phi Rb} \cdot \cos\phi_b}) \tag{19}$$

$$l_{\phi Ra} = \frac{(l_{aa} - x_a) - a_{oa}\sin\phi_a}{\cos\phi_a} \tag{20}$$

$$l_{\phi Rb} = \frac{(l_{ab} - x_b) - a_{ob}\sin\phi_b}{\cos\phi_b} \tag{21}$$

$$\gamma_{1a} = \gamma_a - \phi_a \tag{22}$$

$$\gamma_{1b} = \gamma_b - \phi_b \tag{23}$$

The forces of the front-end springs are calculated using the general relationship between the force and deflection of a non-linear spring depicted in Figure 7 as follows:

$$F_{si} = k_{sij}\delta_i + F_{ij} \tag{24}$$

where k_s and δ represent the stiffness and the deflection of the front-end spring, respectively. The subscript i indicates the spring location (u_R: upper right spring, u_L: upper left spring, l_R: lower right spring and l_L: lower left spring) and the subscript j indicates different stages of the force-deformation characteristics as shown in Figure 7. The stiffness of the spring k_s and the force elements F_{ij} vary according to the different stages of the deflection δ and can be defined as follows:

$$k_{sij} = k_{si1}, \qquad F_{ij} = 0 \qquad 0 \le \delta < \delta_{i1} \tag{25}$$

$$k_{sij} = k_{si2}, \qquad F_{ij} = (k_{si1} - k_{si2})\delta_{i1} \qquad \delta_{i1} \le \delta < \delta_{i2} \tag{26}$$

$$k_{sij} = k_{si3}, \qquad F_{ij} = (k_{si1} - k_{si2})\delta_{i1} + (k_{si2} - k_{si3})\delta_{i2} \qquad \delta_{i2} \le \delta < \delta_{i3} \tag{27}$$

$$k_{sij} = k_{sin}, \qquad F_{ij} = (k_{si1} - k_{si2})\delta_{i1} + (k_{si2} - k_{si3})\delta_{i2} + \ldots + (k_{si(n-1)} - k_{sin})\delta_{i(n-1)} \qquad \delta \ge \delta_{(n-1)} \tag{28}$$

where the deformation of the front-end springs δ_i can be calculated using Figures 4 and 5 as follows:

$$\delta_{uR} = x + \delta_{\theta uR} + \delta_{\phi uR} - \delta_b \tag{29}$$

$$\delta_{uL} = x + \delta_{\theta uL} - \delta_{\phi uL} \tag{30}$$

$$\delta_{lR} = x - \delta_{\theta lR} + \delta_{\phi lR} - \delta_b \tag{31}$$

$$\delta_{lL} = x - \delta_{\theta lL} - \delta_{\phi lL} \tag{32}$$

where δ_θ, δ_φ and δ_b represent the deflection of the front end due to pitching, yawing and the bumper's rotation, respectively and can be calculated as

$$\delta_{\theta uR} = \delta_{\theta uL} = \sqrt{l_f^2 + e_1^2} \cdot \cos(\tan^{-1}(\frac{e_1}{l_f}) - \theta) - l_f \tag{33}$$

$$\delta_{\theta lR} = \delta_{\theta lL} = l_f - [\sqrt{l_f^2 + e_2^2} \cdot \cos(\tan^{-1}(\frac{e_2}{l_f}) + \theta)] \tag{34}$$

$$\delta_{\phi uR} = \delta_{\phi lR} = (l_a - x) - l_{\phi R} \tag{35}$$

$$\delta_{\phi uL} = \delta_{\phi lL} = l_{\phi L} - (l_a - x) \tag{36}$$

$$l_{\phi L} = \frac{(l_a - x) + a_i \sin\phi}{\cos\phi} \tag{37}$$

$$\delta_b = \sqrt{(l_o - l_o \cos\phi_1)^2 + (l_o \cdot \sin\phi_1 + l_{\phi R} \cdot \cos\phi)^2} - l_{\phi R} \tag{38}$$

The suspension forces of the vehicle body can be written as follows:

$$F_{SfR} = k_{SfR}(z - l_f \cdot \sin\theta - b_o \cdot \psi) + c_{fR}(\dot{z} - l_f \cdot \dot{\theta} \cdot \cos\theta - b_o \cdot \dot{\psi}) - u_{fR} \tag{39}$$

$$F_{Sfl} = k_{SfL}(z - l_f \cdot \sin\theta + b_i \cdot \psi) + c_{fL}(\dot{z} - l_f \cdot \dot{\theta} \cdot \cos\theta + b_i \cdot \dot{\psi}) - u_{fL} \tag{40}$$

$$F_{SrR} = k_{SrR}(z + l_r \cdot \sin\theta - b_o \cdot \psi) + c_{rR}(\dot{z} + l_r \cdot \dot{\theta} \cdot \cos\theta - b_o \cdot \dot{\psi}) - u_{rR} \tag{41}$$

$$F_{SrL} = k_{SrL}(z + l_r \cdot \sin\theta + b_i \cdot \psi) + c_{rL}(\dot{z} + l_r \cdot \dot{\theta} \cdot \cos\theta + b_i \cdot \dot{\psi}) - u_{rL} \tag{42}$$

where θ and ψ are the vehicle body pitching and rolling angles, respectively, and $\dot{z}$, $\dot{\theta}$ and $\dot{\psi}$ are the vehicle body vertical, pitching and rolling velocities, respectively. The ASC force

elements (u) are applied in the vertical direction parallel to the existing conventional suspension system.

2.1.2. Forces applied to the vehicle

There are different types of forces which are applied on the vehicle body. These forces are generated by crushing the front-end structure, conventional suspension system due to the movement of the vehicle body and the active control systems such as the ABS and ASC. The free body diagram shown in Figure 2 illustrates these different forces and their directions.

To simulate the upper and lower members of the vehicle front-end structure, multi-stage piecewise linear force-deformation spring characteristics are considered. The non-linear springs used in the multi-body model (ADAMS) (Hogan and Manning, 2007) are taken to generate the n stage piecewise spring's characteristics as shown in Figure 6, while the general relationship between the force and the deflection, Figure 7, is used to calculate the force of the vehicle's front-end. The suspension forces of the vehicle body are also calculated and the detailed equations of these forces are mentioned in section 2.1.1.

Validation of the vehicle dynamics–crash model was established in a previous study by the authors to ensure the validity of the model (Elkady et al., 2012). This is accomplished by comparing the mathematical model results with real test data and the results of the former ADAMS model. The validation showed that the mathematical model results are well matched with the other results.

2.2 Multi-Body Occupant Model

In this section, occupant biodynamics is considered by modelling the occupant mathematically in order to be integrated with the vehicle mathematical model. The occupant model is proposed to be three-body model to capture its dynamic response, rotational events

of the chest and head, due to different crash scenarios. The restraint system consists of seat belt, front and side airbags is presented by different spring-damper systems.

The occupant biodynamic model shown in Figure 8 is developed in this study to evaluate the occupant kinematic behaviour in full and offset frontal crash scenarios. The human body model consists of three bodies with masses m_1, m_2 and m_3. The first body (lower body/pelvis) with mass m_1, represents the legs and the pelvic area of the occupant and it is considered to have a translation motion in the longitudinal direction and rotation motions (pitching, rolling and yawing) with the vehicle body. The second body (middle body/chest), with mass m_2, represents the occupant's abdominal area, the thorax area and the arms, and it is considered to have a translation motion in the longitudinal direction and a rotation motion around the pivot between the lower and middle bodies (pivot 1). The third body (upper body/head), with mass m_3, represents the head and neck of the occupant and it is considered to have a translation motion in the longitudinal direction and a rotational motion around the pivot between the middle and upper bodies (pivot 2).

A rotational coil spring is proposed at each pivot to represent the joint stiffness between the pelvic area and the abdominal area and between the thorax area and the neck/head area. The seatbelt is represented by two linear spring-damper units between the compartment and the occupant. The frontal and side airbags are each represented by two linear spring-damper units.

2.2.1. Equation of motion (EOM) of the human body model

Figures 9 (a), (b), and (c) show the side, top and front views of the occupant model, respectively. For each figure, the positions of the occupant's three bodies are illustrated before and after the crash. Lagrange's equations are used to describe the general motions of the multi-body human model.

The general motions of the multi-body human model are described using Lagrange's equations as follows:

$$\frac{d}{dt}\left(\frac{\partial E}{\partial \dot{x}_1}\right)-\frac{\partial E}{\partial x_1}+\frac{\partial V}{\partial x_1}+\frac{\partial D}{\partial \dot{x}_1}=0 \tag{43}$$

$$\frac{d}{dt}\left(\frac{\partial E}{\partial \dot{\theta}_2}\right)-\frac{\partial E}{\partial \theta_2}+\frac{\partial V}{\partial \theta_2}+\frac{\partial D}{\partial \dot{\theta}_2}=0 \tag{44}$$

$$\frac{d}{dt}\left(\frac{\partial E}{\partial \dot{\theta}_3}\right)-\frac{\partial E}{\partial \theta_3}+\frac{\partial V}{\partial \theta_3}+\frac{\partial D}{\partial \dot{\theta}_3}=0 \tag{45}$$

$$\frac{d}{dt}\left(\frac{\partial E}{\partial \dot{\psi}_2}\right)-\frac{\partial E}{\partial \psi_2}+\frac{\partial V}{\partial \psi_2}+\frac{\partial D}{\partial \dot{\psi}_2}=0 \tag{46}$$

$$\frac{d}{dt}\left(\frac{\partial E}{\partial \dot{\psi}_3}\right)-\frac{\partial E}{\partial \psi_3}+\frac{\partial V}{\partial \psi_3}+\frac{\partial D}{\partial \dot{\psi}_3}=0 \tag{47}$$

where E, V and D are the kinetic energy, potential energy and the Rayleigh dissipation function of the system, respectively. x_1, θ_2, θ_3, ψ_2 and ψ_3 are the longitudinal movement of the occupant's lower body, the rotational angle of the occupant's middle body about y axis, the rotational angle of the occupant's upper body about y axis, the rotational angle of the occupant's middle body about x axis and the rotational angle of the occupant's upper body about x axis, respectively. Hence, $\dot{x}_1$, $\dot{\theta}_2$, $\dot{\theta}_3$, $\dot{\psi}_2$ and $\dot{\psi}_3$ are their associated velocities, respectively.

The kinetic energy of the system can be written as:

$$E=\frac{m_1\cdot v_1^2}{2}+\frac{m_2\cdot v_2^2}{2}+\frac{m_3\cdot v_3^2}{2}+\frac{I_1}{2}\cdot(\dot{\theta}^2+\dot{\phi}^2+\dot{\psi}^2)$$

$$+\frac{I_2}{2}\cdot(\dot{\theta}_2^2+\dot{\psi}_2^2)+\frac{I_3}{2}\cdot(\dot{\theta}_3^2+\dot{\psi}_3^2) \tag{48}$$

where v_1, v_2 and v_3 are the equivalent velocities of the lower, middle and upper bodies of the occupant, respectively. I_1, I_2 and I_3 are the rotational moment of inertia of the lower, middle and upper bodies about the CG of each body, respectively. It is assumed that the rotational moment of inertia of each body around x, y and z axes are the same. $\dot{\theta}$, $\dot{\phi}$ and $\dot{\psi}$ represent the vehicle body pitching, yawing and rolling velocities, respectively. The equivalent velocities of the three bodies of the occupant can be calculated as follows:

$$v_1^2=\dot{X}_{m_1}^2+\dot{Y}_{m_1}^2+\dot{Z}_{m_1}^2 \tag{49}$$

where the displacement of the lower body in x direction can be calculated using Figure 10 as

$$X_{m_1}=x_1+L_1\cdot(\sin\beta-\sin(\beta-\theta)-L_2\cdot(\cos(\zeta-\phi)-\cos\zeta) \tag{50}$$

The velocity of the lower body in x direction can be written as

$$\dot{X}_{m_1}=\dot{x}_1+L_1\cdot\dot{\theta}\cdot\cos(\beta-\theta)-L_2\cdot\dot{\phi}\cdot\sin(\zeta-\phi) \tag{51}$$

The displacement and velocity of the lower body in y direction can be calculated as

$$Y_{m_1}=L_2\cdot(\sin\xi-\sin(\zeta-\phi)+L_3\cdot(\cos\alpha-\cos(\alpha+\psi) \tag{52}$$

$$\dot{Y}_{m_1}=L_2\cdot\dot{\phi}\cdot\cos(\zeta-\phi)+L_3\cdot\dot{\psi}\cdot\sin(\alpha+\psi) \tag{53}$$

the displacement and velocity of the lower body in y direction can be calculated as

$$Z_{m_1}=z+L_1\cdot(\cos(\beta-\theta)-\cos\beta)+L_3\cdot(\sin(\alpha+\psi)-\sin\alpha) \tag{54}$$

$$\dot{Z}_{m_1} = L_1 \cdot \dot{\theta} \cdot \sin(\beta - \theta) + L_3 \cdot \dot{\psi} \cdot \cos(\alpha + \psi) \qquad (55)$$

substituting equations 32, 34 and 36 in equation 30, the equivalent velocity of the lower body can be determined. By repeating the previous steps of these equations (from equation 30 to equation 36), the equivalent velocities of the middle and upper bodies can be calculated.

where X_m is the resultant longitudinal displacement in x direction, Y_m is the resultant vertical displacement in y direction and Z_m is the resultant vertical displacement. (1: lower body, 2: middle body and 3: upper body). L_1 is the distance from the vehicle's y axis to the lower body's CG, L_2 is the distance between the point of impact and the CG of the lower body and L_3 is the distance from the vehicle's x axis to the lower body's CG. It is assumed that L_1, L_2 and L_3 are constant due to the insignificant change of their lengths during the crash. β, ξ, and α are the angles between the vertical centreline of the vehicle z axis and the line between the vehicle's y axis and the CG of the lower body (L_1); the angle between the longitudinal centreline of the vehicle x axis and the line between the point of impact and the CG of the lower body (L_2); and the angle between the vertical centreline of the vehicle z axis and the line between the vehicle's x axis and the CG of the lower body (L_3), respectively.

By substituting the equivalent velocities of the three bodies in equation 4.6, the kinetic energy can be written as follows:

$$E = \frac{1}{2} \cdot (m_1 + m_2 + m_3) \cdot \dot{x}_1^2 + \frac{1}{2} \cdot (m_1 + m_2 + m_3) \cdot \dot{z}^2 + \frac{1}{2} \cdot (m_1 + m_2 + m_3) \cdot L_1^2 \dot{\theta}^2$$

$$+ \frac{1}{2} \cdot (m_1 + m_2 + m_3) \cdot L_2^2 \cdot \dot{\phi}^2 + \frac{1}{2} \cdot (m_1 + m_2 + m_3) \cdot L_3^2 \cdot \dot{\psi}^2 + \left(\frac{m_2}{6} + \frac{m_3}{2} \right) \cdot l_2^2 \cdot \dot{\theta}_2^2$$

$$+ \left(\frac{m_2}{6} + \frac{m_3}{2} \right) \cdot l_2^2 \cdot \dot{\psi}_2^2 + \frac{m_3}{6} \cdot l_3^2 \cdot \dot{\theta}_3^2 + \frac{m_3}{6} \cdot l_3^2 \cdot \dot{\psi}_3^2 + (m_1 + m_2 + m_3) \cdot L_1 \cdot \dot{x}_1 \cdot \dot{\theta} \cdot \cos(\beta - \theta)$$

$$-(m_1+m_2+m_3)\cdot L_2\cdot \dot{x}_1\cdot\dot{\phi}\cdot\sin(\zeta-\phi)$$

$$-(m_1+m_2+m_3)\cdot L_1\cdot L_2\cdot\dot{\theta}\ \cdot\dot{\phi}\cdot\cos(\beta-\theta)\cdot\sin(\zeta-\phi)$$

$$+(m_1+m_2+m_3)\cdot L_2\cdot L_3\cdot\dot{\phi}\cdot\dot{\psi}\cdot\cos(\zeta-\phi)\cdot\sin(\alpha+\psi)$$

$$+(m_1+m_2+m_3)\cdot L_1\cdot\dot{z}\cdot\dot{\theta}\cdot\sin(\beta-\theta)+(m_1+m_2+m_3)\cdot L_3\cdot\dot{z}\cdot\dot{\psi}\cdot\cos(\alpha+\psi)$$

$$-(m_1+m_2+m_3)\cdot L_1\cdot L_3\cdot\dot{\theta}\ \cdot\dot{\psi}\cdot\sin(\beta-\theta)\cdot\cos(\alpha+\psi)+\left(\frac{m_2}{2}+m_3\right)\cdot l_2\cdot\dot{x}_1\cdot\dot{\theta}_2\cdot\cos\theta_2$$

$$-\left(\frac{m_2}{2}+m_3\right)\cdot L_2\cdot l_2\cdot\dot{\phi}\cdot\dot{\psi}_2\cdot\cos(\zeta-\phi)\cdot\cos\psi_2$$

$$-\left(\frac{m_2}{2}+m_3\right)\cdot L_3\cdot l_2\cdot\dot{\psi}\cdot\dot{\psi}_2\cdot\sin(\alpha+\psi)\cdot\cos\psi_2-\left(\frac{m_2}{2}+m_3\right)\cdot l_2\cdot\dot{z}\cdot\dot{\theta}_2\cdot\sin\theta_2$$

$$-\left(\frac{m_2}{2}+m_3\right)\cdot l_2\cdot\dot{z}\cdot\dot{\psi}_2\cdot\sin\psi_2-\left(\frac{m_2}{2}+m_3\right)\cdot L_1\cdot l_2\cdot\dot{\theta}\cdot\dot{\theta}_2\cdot\sin(\beta-\theta)\cdot\sin\theta_2$$

$$-\left(\frac{m_2}{2}+m_3\right)\cdot L_1\cdot l_2\cdot\dot{\theta}\cdot\dot{\psi}_2\cdot\sin(\beta-\theta)\cdot\sin\psi_2$$

$$-\left(\frac{m_2}{2}+m_3\right)\cdot L_3\cdot l_2\cdot\dot{\psi}\cdot\dot{\theta}_2\cdot\cos(\alpha+\psi)\cdot\sin\theta_2$$

$$-\left(\frac{m_2}{2}+m_3\right)\cdot L_3\cdot l_2\cdot\dot{\psi}\cdot\dot{\psi}_2\cdot\cos(\alpha+\psi)\cdot\sin\psi_2+\left(\frac{m_2}{4}+m_3\right)\cdot l_2^2\cdot\dot{\theta}_2\cdot\dot{\psi}_2\cdot\sin\theta_2\cdot\sin\psi_2$$

$$+\frac{m_3}{2}\cdot l_3\cdot\dot{x}_1\cdot\dot{\theta}_3\cos\theta_3+\frac{m_3}{2}\cdot L_1\cdot l_3\cdot\dot{\theta}\cdot\dot{\theta}_3\cdot\cos(\beta-\theta)\cdot\cos\theta_3$$

$$-\frac{m_3}{2}\cdot L_2\cdot l_3\cdot\dot{\phi}\cdot\dot{\theta}_3\cdot\sin(\zeta-\phi)\cdot\cos\theta_3+\frac{m_3}{2}\cdot l_2\cdot l_3\cdot\dot{\theta}_2\cdot\dot{\theta}_3\cdot\cos\theta_2\cdot\cos\theta_3$$

$$-\frac{m_3}{2}\cdot L_2\cdot l_3\cdot\dot{\phi}\cdot\dot{\psi}_3\cdot\cos(\zeta-\phi)\cdot\cos\psi_3-\frac{m_3}{2}\cdot L_3\cdot l_3\cdot\dot{\psi}\cdot\dot{\psi}_3\cdot\sin(\alpha+\psi)\cdot\cos\psi_3$$

$$+\frac{m_3}{2}\cdot l_2\cdot l_3\cdot\dot{\psi}_2\cdot\dot{\psi}_3\cdot\cos\psi_2\cdot\cos\psi_3-\frac{m_3}{2}\cdot l_3\cdot\dot{z}\cdot\dot{\theta}_3\cdot\sin\theta_3-\frac{m_3}{2}\cdot l_3\cdot\dot{z}\cdot\dot{\psi}_3\cdot\sin\psi_3$$

$$-\frac{m_3}{2}\cdot L_1\cdot l_3\cdot\dot{\theta}\cdot\dot{\theta}_3\cdot\sin(\beta-\theta)\cdot\sin\theta_3-\frac{m_3}{2}\cdot L_1\cdot l_3\cdot\dot{\theta}\cdot\dot{\psi}_3\cdot\sin(\beta-\theta)\cdot\sin\psi_3$$

$$-\frac{m_3}{2}\cdot L_3\cdot l_3\cdot\dot{\psi}\cdot\dot{\theta}_3\cdot\cos(\alpha+\psi)\cdot\sin\theta_3-\frac{m_3}{2}\cdot L_3\cdot l_3\cdot\dot{\psi}\cdot\dot{\psi}_3\cdot\cos(\alpha+\psi)\cdot\sin\psi_3$$

$$+\frac{m_3}{2}\cdot l_2\cdot l_3\cdot\dot{\theta}_2\cdot\dot{\theta}_3\cdot\sin\theta_2\cdot\sin\theta_3+\frac{m_3}{2}\cdot l_2\cdot l_3\cdot\dot{\theta}_2\cdot\dot{\psi}_3\cdot\sin\theta_2\cdot\sin\psi_3$$

$$+\frac{m_3}{2}\cdot l_2\cdot l_3\cdot\dot{\psi}_2\cdot\dot{\theta}_3\cdot\sin\psi_2\cdot\sin\theta_3+\frac{m_3}{2}\cdot l_2\cdot l_3\cdot\dot{\psi}_2\cdot\dot{\psi}_3\cdot\sin\psi_2\cdot\sin\psi_3$$

$$m_3\cdot l_3^2\cdot\dot{\theta}_3\cdot\dot{\psi}_3\cdot\sin\theta_3\cdot\sin\psi_3 \qquad (56)$$

where l_2 and l_3 are the middle body and upper body lengths, respectively. Using Figure 9 the potential energy of the system can be written as

$$V=m_1\cdot g\cdot[h+z+L_1\cdot(\cos(\beta-\theta)-\cos\beta)]+m_2\cdot g\cdot[h+z+L_1\cdot(\cos(\beta-\theta)-\cos\beta)$$

$$+\frac{l_2}{2}\cdot\cos\theta_2-\frac{l_2}{2}\cdot(1-\cos\psi_2)]+m_3\cdot g\cdot[h+z+L_1\cdot(\cos(\beta-\theta)-\cos\beta)+l_2\cdot\cos\theta_2$$

$$-l_2\cdot(1-\cos\psi_2)+\frac{l_3}{2}\cdot\cos\theta_3-\frac{l_3}{2}\cdot(1-\cos\psi_3)]+\frac{1}{2}\cdot[F_{k1}\cdot\delta_1+F_{k2}\cdot\delta_2+F_{k3}\cdot\delta_3+F_{k4}\cdot\delta_4$$

$$+F_{k5}\cdot\delta_5+F_{k6}\cdot\delta_6+F_{k12\theta}\cdot\delta_{12\theta}+F_{k12\psi}\cdot\delta_{12\psi}+F_{k23\theta}\cdot\delta_{23\theta}+F_{k23\psi}\cdot\delta_{23\psi}] \qquad (57)$$

where h is the vehicle's CG height and z is the vertical displacement of the vehicle body. F_{k1}, F_{k2}, F_{k3}, F_{k4}, F_{k5} and F_{k6} are the forces generated from the lower seatbelt spring, the upper seatbelt spring, the lower frontal airbag spring, the upper frontal airbag spring, the lower side airbag spring, the upper side airbag spring, respectively. $F_{k12\theta}$ and $F_{k12\psi}$ are the forces generated from the rotational spring between the middle and lower body around y and x axes, respectively; $F_{k23\theta}$ and $F_{k23\psi}$ are the forces generated from the rotational spring between the upper and middle body around y and x axes, respectively. δ_1, δ_2, δ_3, δ_4, δ_5 and δ_6 represent the total deflection of the lower seatbelt spring, of the upper seatbelt spring, of the lower frontal airbag spring, of the upper frontal airbag spring, of the lower side airbag spring, of the upper side airbag spring, respectively. $\delta_{12\theta}$ and $\delta_{12\psi}$, $\delta_{23\theta}$ and $\delta_{23\psi}$ are the deflection of the rotational spring between the lower and middle body around y and x axes and deflection of the rotational spring between the middle and upper body around y and x axes, respectively.

The Rayleigh dissipation function can be written as follows:

$$D = \frac{1}{2} \cdot [F_{c1} \cdot \dot{\delta}_1 + F_{c2} \cdot \dot{\delta}_2 + F_{c3} \cdot \dot{\delta}_3 + F_{c4} \cdot \dot{\delta}_4 + F_{c5} \cdot \dot{\delta}_5 + F_{c6} \cdot \dot{\delta}_6] \qquad (58)$$

where F_{c1}, F_{c2}, F_{c3}, F_{c4}, F_{c5} and F_{c6} are the forces generated from the lower seatbelt, the upper seatbelt, the lower frontal airbag, the upper frontal airbag, the lower side airbag, and the upper side airbag dampers, respectively. $\dot{\delta}_1$, $\dot{\delta}_2$, $\dot{\delta}_3$, $\dot{\delta}_4$, $\dot{\delta}_5$, and $\dot{\delta}_6$ are the associated velocities of the δ_1, δ_2, δ_3, δ_4, δ_5 and δ_6, respectively.

The forces F_{ki} and F_{ci} (where i= 1, 2, ...) are calculated as

$$F_{ki} = k_i \cdot \delta_i \qquad (59)$$

$$F_{ci} = c_i \cdot \dot{\delta}_i \qquad (60)$$

In order to get the components of the equations 1, 2, 3, 4 and 5, the differentiations of the kinetic energy, potential energy and Rayleigh dissipation function are determined. To solve these equations, they need to be re-arranged in an integratable form and then rewritten in a matrix form as follows:

$$[\mathrm{A}]\cdot[\ddot{\mathrm{B}}]=[\mathrm{C}] \tag{61}$$

where the $[\ddot{\mathrm{B}}]=\begin{bmatrix}\ddot{x}_1 & \ddot{\theta}_2 & \ddot{\theta}_3 & \ddot{\psi}_2 & \ddot{\psi}_3\end{bmatrix}^{\mathrm{T}}$.

The final form then can be written as:

$$[\ddot{\mathrm{B}}]=[\mathrm{A}]^{-1}\cdot[\mathrm{C}] \tag{62}$$

Different occupant bodies' responses (x_1, θ_2, θ_3, ψ_2 and ψ_3) can be determined by solving equation 62 numerically.

The occupant model has been validated by the authors in previous work by comparing its results with the former finite element human model and crash test (Elkady, 2012). The validation showed that the results from the mathematical model and the previous results are in good agreement.

3. NUMERICAL SIMULATIONS

Seven different cases of VDCS are investigated in this section and their associated results are compared with the free rolling case scenario. These different VDCS cases are described as follows:

Case 1: Free rolling - in this case the vehicle collides with a barrier/vehicle without applying any types of control.

Case 2: ABS - in this case the anti-lock braking system is applied before and during the collision.

Case 3: ABS + ASC - the ASC system is integrated with the ABS to increase the normal force on the vehicle body and hence increase the braking force.

Case 4: ABS + frontal active suspension control (FASC) - the ASC system is integrated with the ABS on the front wheels only.

Case 5: ABS + anti-pitch control (APC) - the APC system is integrated with the ABS using the ACS to keep the vehicle in a horizontal position before the crash by applying an active force element on the front and rear wheels in upward and downward directions, respectively.

Case 6: ABS + UPC - in this case, the vehicle is taken a reverse pitching angle before crash using an ASC system.

Case 7: ABS DYC - the braking force is used to be applied to individual wheels to reduce the yawing moment of the vehicle body.

3.1 Primary Impact Results

The primary impact simulation results for offset vehicle-to-vehicle crash scenario are demonstrated in this section. The values of different parameters used in numerical simulations are given in Table 1 (Alleyne, 1997). The effect of the different cases of VDCS on vehicle collision mitigation is also investigated. In addition, the effect of the control systems on the other vehicle (vehicle b) is discussed. Figure 11 shows the impacted side of the front-end structure's deformation-time histories for vehicle (a) for all different VDCS cases. It is noticed that the deformation increased to reach its maximum value (different for each case) and then decreased slightly due to front-end springs rebound. The minimum

deformation is obtained in the case 3 when the ASC is applied along with ABS. The maximum reduction of 50 mm is observed in this case and a reduction of 30 mm is shown in case 6, while a reduction of about 25 mm is obtained in cases 2, 4 and 5 compared with the free rolling case. On the other hand, case 7 (ABS + DYC) produced a higher deformation with a total reduction of about 15 mm. The integrated control of the ASC with the ABS aims to increase the braking force by increasing the vertical load to obtain a minimum stopping distance. It is worth mentioning that the application of the ASC control system (case 3) helps reducing the maximum deformation of the front-end structure as shown in Figure 11.

Figure 12 shows the front-end structure's deformation-time histories for vehicle (b) in all different VDCS cases. Because the two vehicles are identical and both collide at the same speed, it is clearly shown that the simulation results of the free rolling case are exactly the same. The maximum deformation is almost the same with very small and insignificant values for all cases of VDCS, and this means the control systems have no great effect on the front-end deformation of the other vehicle during the full frontal collision.

The deceleration – time histories of the vehicle body for all cases for vehicle (a) are presented in Figure 13. The deceleration-time history can be divided to three stages. The first stage represents the increase of the vehicle's deceleration before the front left wheel reach the barrier. In this stage the highest deceleration value is observed in case 3. In the other cases, a slight higher deceleration is also noticed compared with the free rolling case. In the second stage, the front left wheel reaches the barrier and stop moving, therefore its braking effects is vanished. At the beginning of this stage a rapid reduction in the vehicle body deceleration occurs (arrow 1, Figure 13); this deceleration drop does not appear in the free rolling case while there is no applied braking. During the second stage, it is noticed that the minimum deceleration is still in case 1, while the maximum deceleration is almost the same for all other

cases. At the end of this stage, the vehicle stops and starts moving in the opposite direction. In addition, the braking force changes its direction and another drop in the vehicle deceleration is noticed as shown in Figure 13, (arrow 2). At the third stage, a condition of allowing the front-end springs to be rebounded for a very short time is applied during the simulation analysis. During this stage, the vehicle moves back and the deformation of the front-end decreases as shown in Figure 13. At the end of this stage, the non-linear front-end springs are deactivated and the vehicle's deceleration suddenly dropped to a value of zero. This fast drop is due to the assumption of immediate stopping the effect front-end springs after a very short time of rebound.

An insignificant increase of the vehicle deceleration in all VDCS cases is observed in the other vehicle (b) compared with the free rolling case as shown in Figure 14. The maximum values of the vehicle deceleration in vehicle (b) are also almost the same for all the VDCS cases.

Figure 15 shows the vehicle's pitch angle-time histories for all cases of vehicle (a). The VDCS is applied 1.5 second before the collision, therefore, the vehicle body impacts the barrier at different values of pitch angles according to each case as shown in Figure 15. The vehicle's pitch angle then reaches its maximum values (normally after the end of the crash) according to each case. Following this, the pitch angle reduced to reach negative values and then bounces to reach its steady-state condition. In the offset crash scenario, vehicle body pitching angle is generated due to the difference in impact forces between the upper and lower front-end members of the impacted side in the free rolling case. Additional pitching moment is generated from the braking force in the other VDCS cases. The maximum pitch angle is observed in case 2 followed by case 7, 4, 1, 5, 3 and finally case 6. In case 6, a

notable reduction of about 6.5 deg compared with case 1 and about 12 deg, compared with case 2 are observed.

A rolling moment of the vehicle body is generated during the crash due to the different values of the component of the left frontal springs' forces in y direction and from the friction between the ground and the tyres due to the yaw motion. At the end of the collision, the pitching and rolling moments are ended and the vehicle is controlled by the tyres and suspension forces. The vehicle's rear wheels left the ground during the vehicle pitching and the left wheels (front and rear) left the ground as well during the vehicle rolling. At this moment, three wheels of the vehicle are not contacted with the ground with different distances. This explains the different sudden changes of the vehicle pitching acceleration when each wheel re-contact the ground (look at the arrows referred to case 1 in Figure 16).

The vehicle body pitching acceleration is also depicted in Figure 16 for all seven cases for vehicle (a). The vehicle maximum pitching acceleration is observed in cases 2, 4 and 7, whilst the lowest value is detected in case 6 (ABS + UPC). Compared with case 1 (free rolling) and case 2 (ABS), a reduction of about 670 deg/s2 and about 950 deg/s2, respectively, are obtained in case 6 (ABS + UPC).

Similarly, the pitch angle and pitch acceleration-time histories for vehicle (b) are depicted in Figures 17 and 18, respectively. It is noticed that there is no difference between the results of the seven crash scenarios. That means the different applied cases of the VDCS on vehicle (a) do not affect the pitching event of vehicle (b) in case of offset collision.

Figure 19 shows the vehicle yaw velocity-time histories for all seven cases of vehicle (a). The vehicle yaw velocity is equal to zero before the crash, then it changes in three different stages: firstly, it increases rapidly to reach its maximum value; secondly, it decreases slowly for a different period of time related to each case; and thirdly it decreases gradually to reach

zero. In the first stage, the rapid increase in the yaw velocity is due to the high yawing acceleration (see Figure 20) caused by the one side impacted spring. At the end of the collision, the rear wheels left the ground due to the vehicle pitching and the front-left wheel left the ground due to the vehicle rolling and hence the vehicle is controlled by the front-right wheel only. In the second stage, the decrease in the vehicle's yaw velocity occurred due to the friction force between the front-rear tyre and the ground. The period of this stage is different for each case and it mainly depends on the maximum pitching angle. During the second stage, the front-left wheel re-contacts the ground. Stage 3 begins when the rear wheels start contacting the ground generating yaw moments in the opposite direction. This is causing a reduction of the vehicle yawing velocity with a higher rate than the decreasing of velocity rate in the second stage. Because of the maximum vehicle front-end deformation is observed in case 1 (free rolling) as shown in Figure 11, the greatest peak of yaw velocity appears in the same case as shown in Figure 19. A reduction of the maximum yawing velocity (10 deg/s) is observed in cases 3 and 6, while a reduction of about 5 deg/s is obtained in the other cases of VDCS.

Vehicle body yaw acceleration-time histories are depicted in Figure 20. The maximum yaw acceleration is observed in case 1 (free rolling) and the minimum yaw acceleration is also observed in cases 3 and 6. At the end of the collision, the vehicle is controlled by the front-left wheel only, as mentioned before, trying to hinder the yawing motion. Accordingly, a negative yawing acceleration is generated with different small values related to each case as shown in Figure 20 (arrow 1). These negative values of the vehicle yaw acceleration increase slowly with time producing two sudden drops of acceleration (arrow 2) once the right-rear wheel and the left-rear wheel re-contact the ground, respectively. These drops are not shown in case 6 because the rear wheels do not leave the ground in this case. When the vehicle

yawing ends and the yaw speed reaches zero, the yaw acceleration returns to zero as well as shown in Figure 20 (arrow 3).

Figure 21 shows the vehicle body yaw angle – time histories for all cases of vehicle (a). It is found that the maximum yaw angle of 49.3 deg is noticed in case 2 (ABS) while the minimum yaw angle of 36.8 deg is noticed in case 6 (ABS + UP). The maximum value of the vehicle yaw angle depends on the maximum yaw acceleration and the vehicle pitch angle for each case. It is worth mentioning that reducing the maximum vehicle body yaw angle reduces the risk of the car side-impact by any obstacles on the road. Following the yawing analysis, it can be said that the best set of the vehicle dynamic control is to apply case 6 (ABS + UPC) since the minimum yaw angle and acceleration are obtained in this case.

The yawing event of the vehicle (b), which is not equipped by the VDCS, is affected by vehicle (a) once different control systems are applied. The maximum yaw velocity of the vehicle (b) is increased in all cases compared with the free rolling case, except in case 6, as shown in Figure 22. Figure 23 shows the yaw acceleration of the vehicle (b). It is observed that the maximum yaw acceleration is also increased in all cases compared with the free rolling case by different values related to each case. In the same manner, the maximum yaw angle of the vehicle (b) is increased in all cases by different values (from 1.5 to 2 deg) related to each case, except in case 6 as shown in Figure 24.

3.2 Secondary Impact Results

The secondary impact simulation results for offset vehicle-to-vehicle crash scenario are demonstrated in this section. The values of different parameters used in numerical simulations are given in Table 2. The values m_1, m_2, m_3, l_2, l_3, k_{12} and k_{23} have been taken from (Ilie and Tabacu, 2010). Figure 25 shows the occupant's pelvis relative displacement for vehicle (a). It is shown that it increases forward to reach its maximum position and then

returns due to the lower seatbelt springs. It is observed that there are insignificant differences between the values of the maximum relative displacement of the occupant's pelvis. Figure 26 shows the lower-body deceleration for all cases of vehicle (a). It is shown that it increases during the collision to reach its maximum values at the end of impact and then reduces after the effect of collision is ended. The sudden decrease of the deceleration (arrow 1 in Figure 26) is due to the reverse direction of the braking force at the end of the impact when the vehicle changes its direction and starts to move backward. It observed that the maximum deceleration is almost the same for all cases with very small differences. These small differences mean that the VDCS do have an insignificant effect on the pelvis relative displacement and deceleration.

The rotation angle of the occupant's chest about y axis for all cases for vehicle (a) is shown in Figure 27. The occupant's chest starts the collision with different rotational angles according to each case. The occupant takes this angle in the period of 1.5 sec prior collisions when the VDCS is applied. After that, the rotational angle of the occupant's chest remains constant for about 0.03 sec, then it increased to reach its maximum value after the end of the collision. The maximum rotation angle is observed in cases 2, 4 and 7 while the minimum one is observed in case 6 (ABS + UPC). Figure 28 shows the rotational acceleration about y axis of the occupant's chest. The chest rotational acceleration increases gradually to reach its maximum positive value and then reduces to reach its maximum negative value. The maximum positive rotational acceleration is monitored in case 1 and the minimum one occurred in case 5, while the maximum negative rotational acceleration is shown in case 6 and the minimum is in case 2 and 7.

The rotation angle of the occupant's head about y axis is depicted in Figure 29. The head rotation angle increases rapidly for a period of time, which occurred during the increase of

the chest rotation. And then, it increases fast due to the return of the occupant's chest to reach its peak value (maximum value). The peak value of the head rotational angle is observed in cases 2, 4 and 7, while the minimum one is detected in case 6. Figure 30 shows the rotational acceleration of the occupant's head. The acceleration increases with a different manner according to each case to reach its maximum value. These maximum values occurred in different time related to each case. In other words, the maximum acceleration in cases 1, 3 and 6 occurs approximately at 0.07 sec, while in the other cases it occurs approximately at 0.08 sec. The minimum negative acceleration is observed in cases 2 and 7, while the maximum negative values are seen in cases 1 and 6.

The rotation angle about x axis of the occupant's chest for all cases of vehicle (a) is depicted in Figure 31. When the occupant's chest reaches its maximum rotational angle, it stays at this position for a period of time while the vehicle rotates around the point of impact. The maximum rotation angle is observed in case 1 (free rolling) while the minimum angle is observed in cases 3 and 6 (ABS + ASC and ABS + UPC). Figure 32 shows the rotational acceleration of the occupant's chest about x axis for all 6 cases for vehicle (a). The first sudden change in this acceleration is due to the activation of the side airbag, while the second one is due to the reverse braking force (arrows 1 and 2, respectively). The third sudden change of the chest acceleration (arrow 3) is due to the deactivation of the vehicle's front-end springs, which causes a sudden decrease of the vehicle pitching, yawing and rolling. The maximum positive rotational acceleration of the occupant's chest about x axis is observed in cases 1 and 7, while the minimum value occurs in cases 3. The maximum negative rotational acceleration happens in cases 1 and 4 and the minimum is observed in case 3. These negative acceleration values occur due to the force generated by the lower spring-damper system of the side airbag.

The rotation angle about x axis of the occupant's head for vehicle (a) is shown in Figure 33. At the beginning of the collision, while the chest takes a positive acceleration and starts rotating towards the vehicle's side door, the head takes a different negative small rotation value related to each case, all these values are close to 5 deg. The positive maximum value of the head rotational angle is observed in case 6, while the minimum peak angle is seen in cases 2, 3, 4 and 7. Figure 34 shows the rotational acceleration about x axis of the occupant's head for all cases. The effect of the reverse braking force is observed at the end of the collision (arrow 1 in Figure 34). The maximum positive acceleration (in the period from 0.06 to 0.1 sec) is almost the same for all cases, while the maximum negative acceleration (in the period from 0.1 to 0.16 sec), caused by the side airbag force, is observed in cases 1 with relatively a higher value. The minimum negative acceleration is detected in cases 2, 4, 5 and 7.

Figures 35 and 36 show the occupant's pelvis relative displacement and deceleration, respectively for vehicle (b). It is shown that the occupant's pelvis relative displacement and deceleration are insignificantly affected by the application of VDCS on the other vehicle (vehicle (a)). There are very small and insignificant increases, especially on the peak values, for all cases compared with the free rolling case.

Figures 37 and 38 show the occupant's chest rotational angle for vehicle (b) and its acceleration about y axis, respectively. It observed that there are no changes in the rotational angle; however, there are small variations among the different cases on the occupant's chest acceleration from 0.13 to 0.15 sec. These variations are also very small and insignificant.

Figure 39 shows the occupant's head rotational angle about y axis for the occupant in vehicle (b). It is clearly shown that there are very small differences of the maximum rotational angle according to the different cases. Figure 40 shows the occupant's head rotational acceleration about y axis for all cases. From this figure, a clear difference in the head rotational

acceleration is detected at 0.135 sec. When the VDCS is applied, the maximum head rotational acceleration becomes higher than the one in the free rolling case with different values from 5 to 15 kdeg/sec^2 related to each case; and the maximum head rotational acceleration is shown in case 2.

The occupant's chest rotational angle about x axis for vehicle (b) is shown in Figure 41. Compared with the free rolling case, the rotational angle of the chest is increased by small values from about 0.2 deg in case 6 to about 2 degs in cases 2 and 4. Figure 42 illustrates the occupant's chest acceleration about the x axis. Very small increases of the chest rotational acceleration are observed when the VDCS are applied at the periods from 0.04 to 0.09 sec and from 0.13 to 0.15 sec. This increase in the chest rotational acceleration ranges between 300 to 800 deg/sec2, however, these are not significant values.

The maximum occupant's head rotational angle about x axis is also increased when any of the VDCS is applied as shown in Figure 43. This increase ranges between 0.2 to 1 deg, and this is not a significant value. The maximum head rotational angle is observed in case 2, while the minimum value is detected in case 1. The maximum positive acceleration of the occupant's head about x axis is almost the same. However, the maximum negative head rotational acceleration is increased when the VDCS are applied. In case 6 the head rotational acceleration is increased by about 5 kdeg/s^2, while the highest increase value is observed in case 2 by about 15 kdeg/s^2.

4. CONCLUSIONS

Development of a new 6-DOF vehicle dynamics/crash mathematical model and three dimensional-three-mass occupant mathematical model have been represented to study the effect of vehicle dynamic control systems (VDCS) on vehicle crash at offset frontal vehicle-to-vehicle collision. The models presented here would be very useful in the early design

stages for assessing the crash worthiness performance of the vehicle and for selecting appropriate vehicle parameters. From the numerical simulations, it can be said that the VDCS can improve the vehicle crash situation and the occupant behaviour. The different cases applied in this paper have a different effect on the vehicle and its occupant. It is shown that the crash event gets worse related to the vehicle (b), based on higher values of vehicle deceleration, pitching angle and acceleration, etc. However, these higher values are very small and insignificant.

Acknowledgment: The authors would like to thank the Egyptian Government and the Faculty of Engineering, Ain Shams University for supporting this research.

We also acknowledge with sadness, the contribution of Prof. Dave Crolla who has passed away during the period of this research.

REFERENCES

Alleyne, A., 1997. Improved Vehicle Performance Using Combined Suspension and Braking Forces. Vehicle System Dynamics, 27, 4, pp. 235–265.

Chang, J.M., Ali, M., Craig, R., Tyan, T., El-bkaily, M., Cheng, J., 2006. Important Modeling Practices in CAE Simulation for Vehicle Pitch and Drop. SAE International, Warrendale, PA, SAE Technical Paper 2006-01-0124.

Elmarakbi, A. and Zu, J. 2007. Incremental Harmonic Balance Method for Analysis of Standard/Smart Vehicles-to-Rigid Barrier Frontal Collision. International journal of vehicle safety 2 (3), 288-315.

Elmarakbi, A. and Zu, J. 2005. Crashworthiness Improvement of Vehicle-to-Rigid Fixed Barrier in Full Frontal Impact using Novel Vehicle's Front-End Structures. International journal of automotive technology 6 (5), 491-499.

Emori, R. I., 1968. Analytical Approach to Autombile Collisions. SAE International, Warrendale, PA. Technical Paper 680016.

Hogan, I., Manning, W., 2007. The Use of Vehicle Dynamic Control Systems for Automotive Collision Mitigation. 3rd Institution of Engineering and Technology Conference on Automotive Electronics, USA, 28-29 June 2007, pp. 1 –10.

Ilie, S., Tabacu, Ş., 2010. Study of the Occupant's Kinematics during the Frontal Impact. Ann Oradea Univ, Fascicle Managmt Technol Engng 2007, 6, 16, pp. 542–551

Jansson, J., Gustafsson, F., Ekmark, J., 2002a. Decision Making For Collision Avoidance Systems. SAE International, Warrendale, PA, SAE Technical Paper 2002-01-0403

Kamal, M.M., 1970. Analysis and Simulation of Vehicle to Barrier Impact. SAE International, Warrendale, PA, Technical Paper 700414

Khattab, A., 2010. Steering system and method for independent steering of wheels (Ph.D. Thesis), The department of Mechanical and Industrial Engineering, Concordia University Montreal, Quebec, Canada.

Kim, H.-S., 2002. New Extruded Multi-Cell Aluminum Profile For Maximum Crash Energy Absorption And Weight Efficiency. Thin-Walled Structures 40, 4, pp. 311–327.

Sugimoto, Y., Sauer, C., 2005. Effectiveness Estimation Method for Advanced Driver Assistance System and Its Application to Collision Mitigation Brake System. Proceeding 19th International Technology Conference, Enhanced Safety Vehicles. pp. 1–8.

Tamura, M., Inoue, H., Watanabe, T., Maruko, N., 2001. Research on a Brake Assist System with a Preview Function. SAE International, Warrendale, PA, SAE Technical Paper 2001-01-0357

Witteman, W.J., 1999. Improved Vehicle Crashworthiness Design by Control of the Energy Absorption for Different Collision Situations. (Ph.D. Thesis), Technische University.

Witteman, W.J., Kriens, R.F.C., 1998. Modeling of an Innovative Frontal Car Structure: Similar Deceleration Curves at Full Overlap, 40 Percent Offset and 30 Degrees Collisions. Proceedings of 16th International Technical Conference on the Enhanced Safety of Vehicles, Held Windsor, Ontario, Canada, 31 May - 4 June 1998, pp. 194-212

Yu, F., Feng, J.Z., Li, J., 2002. A Fuzzy Logic Controller Design for Vehicle Abs with an On-Line Optimized Target Wheel Slip Ratio. International Journal of Automotive Technology 3, 4, pp. 165–170.

Yue, C., Butsuen, T., Hedrick, J.K., 1988. Alternative Control Laws for Automotive Active Suspensions. American Control Conference, USA, 15-17 June 1988, pp. 2373 –2378.

List of tables

Table 1: The values of the different parameters, which are used in the simulations

Table 2: The values of the different parameters, which are used in the simulations

List of figures

Figure 1: 6-DOF vehicle dynamics/crash mathematical model

Figure 2: Free body diagram of the mathematical model

Figure 3 (a): Vehicle model before crash (offset frontal impact)

Figure 3 (b): Vehicle model after crash (offset frontal impact)

Figure 4: Illustration drawing of the front-end deformation due to vehicle pitching

(---- Before pitching —— After pitching)

Figure 5: Illustration drawing of the front-end deformation due to vehicle yawing

(---- Before yawing —— After yawing)

Figure 6: Force deformation characteristics for upper and lower rails

Figure 7: General piecewise force-deformation characteristics

Figure 8: Multi-body occupant model

Figure 9 (a): Side view of the occupant model

Figure 9 (b): Top view of the occupant model (POI: Point of Impact)

Figure 9 (c): Frontal view of the occupant model

Figure 10: A schematic diagram of the occupant's lower body movement during impact

Figure 11: Deformation of the front-end structure (Offset frontal vehicle-to-vehicle impact) vehicle (a)

Figure 12: Deformation of the front-end structure (Offset frontal vehicle-to-vehicle impact), vehicle (b)

Figure 13: Vehicle body deceleration (Offset frontal vehicle-to-vehicle impact), vehicle (a)

Figure 14: Vehicle body deceleration (Offset frontal vehicle-to-vehicle impact), vehicle (b)

Figure 15: Vehicle body pitch angle (Offset frontal vehicle-to-vehicle impact), vehicle (a)

Figure 16: Vehicle body pitch acceleration (Offset frontal vehicle-to-vehicle impact), vehicle (a)

Figure 17: Vehicle body pitch angle (Offset frontal vehicle-to-vehicle impact), vehicle (b)

Figure 18: Vehicle body pitch acceleration (Offset frontal vehicle-to-vehicle impact), vehicle

Figure 19: Vehicle body yaw velocity (Offset frontal vehicle-to-vehicle impact), vehicle (a)

Figure 20: Vehicle body yaw acceleration (Offset frontal vehicle-to-vehicle impact), vehicle (a)

Figure 21: Vehicle body yaw angle (Offset frontal vehicle-to-vehicle impact), vehicle (a)

Figure 22: Vehicle body yaw velocity (Offset frontal vehicle-to-vehicle impact), vehicle (b)

Figure 23: Vehicle body yaw acceleration (Offset frontal vehicle-to-vehicle impact), vehicle

Figure 24: Vehicle body yaw angle (Offset frontal vehicle-to-vehicle impact), vehicle (b)

Figure 25: Occupant's pelvis displacement (Offset frontal vehicle-to-vehicle impact), vehicle

Figure 26: Occupant's pelvis deceleration (Offset frontal vehicle-to-vehicle impact), vehicle

Figure 27: Rotational angle of the occupant's chest about y axis (Offset frontal vehicle-to-vehicle impact), vehicle (a)

Figure 28: Rotational acceleration of the occupant's chest about y axis (Offset frontal vehicle-to-vehicle impact), vehicle (a)

Figure 29: Rotational angle of the occupant's head about y axis (Offset frontal vehicle-to-vehicle impact), vehicle (a)

Figure 30: Rotational acceleration of the occupant's head about y axis (Offset frontal vehicle-to-vehicle impact), vehicle (a)

Figure 31: Rotational angle of the occupant's chest about x axis (Offset frontal vehicle-to-vehicle impact), vehicle (a)

Figure 32: Rotational acceleration of the occupant's chest about x axis (Offset frontal vehicle-to-vehicle impact), vehicle (a)

Figure 33: Rotational angle of the occupant's head about x axis (Offset frontal vehicle-to-vehicle impact), vehicle (a)

Figure 34: Rotational acceleration of the occupant's head about x axis (Offset frontal vehicle-to-vehicle impact), vehicle (a)

Figure 35: Occupant's pelvis displacement (Offset frontal vehicle-to-vehicle impact), vehicle

(b)

Figure 36: Occupant's pelvis deceleration (Offset frontal vehicle-to-vehicle impact), vehicle (b)

Figure 37: Rotational angle of the occupant's chest about y axis (Offset frontal vehicle-to-vehicle impact), vehicle (b)

Figure 38: Rotational acceleration of the occupant's chest about y axis (Offset frontal vehicle-to-vehicle impact), vehicle (b)

Figure 39: Rotational angle of the occupant's head about y axis (Offset frontal vehicle-to-vehicle impact), vehicle (b)

Figure 40: Rotational acceleration of the occupant's head about y axis (vehi Offset frontal vehicle-to-vehicle impact), vehicle (b)

Figure 41: Rotational angle of the occupant's chest about x axis (Offset frontal vehicle-to-vehicle impact), vehicle (b)

Figure 42: Rotational acceleration of the occupant's chest about x axis (Offset frontal vehicle-to-vehicle impact), vehicle (b)

Figure 43: Rotational angle of the occupant's head about x axis (Offset frontal vehicle-to-vehicle impact), vehicle (b)

Figure 44: Rotational acceleration of the occupant's head about x axis (Offset frontal vehicle-to-vehicle impact), vehicle (b)

List of Figures

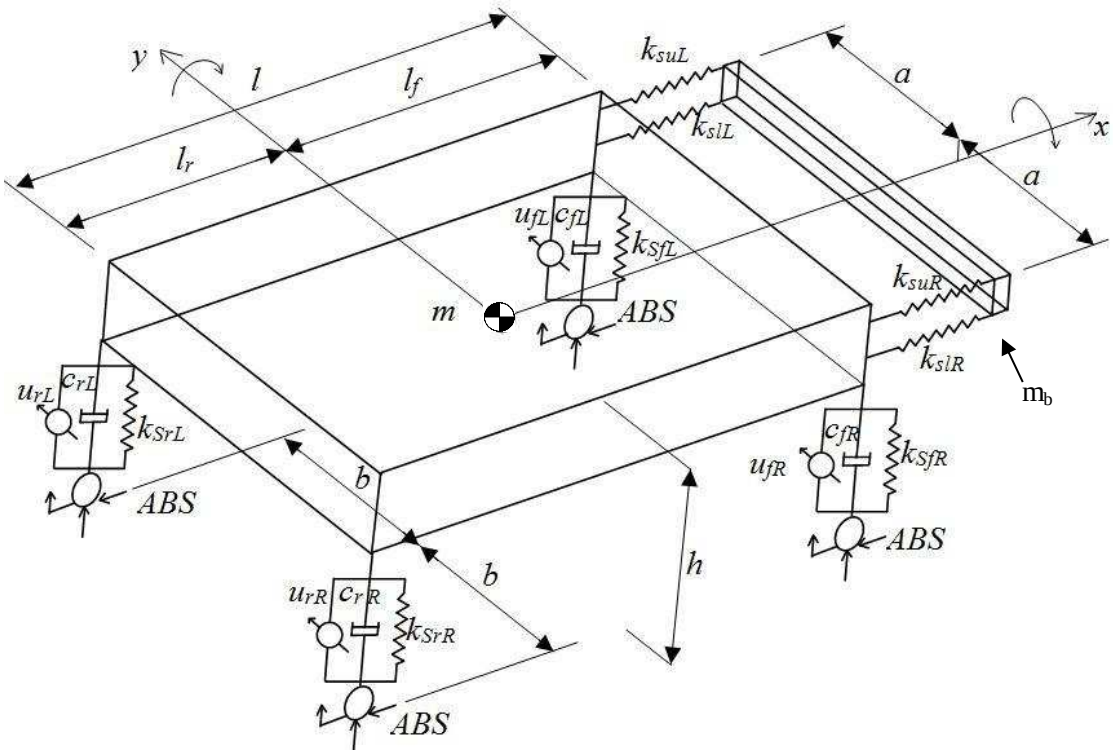

Figure 1: 6-DOF vehicle dynamics/crash mathematical model

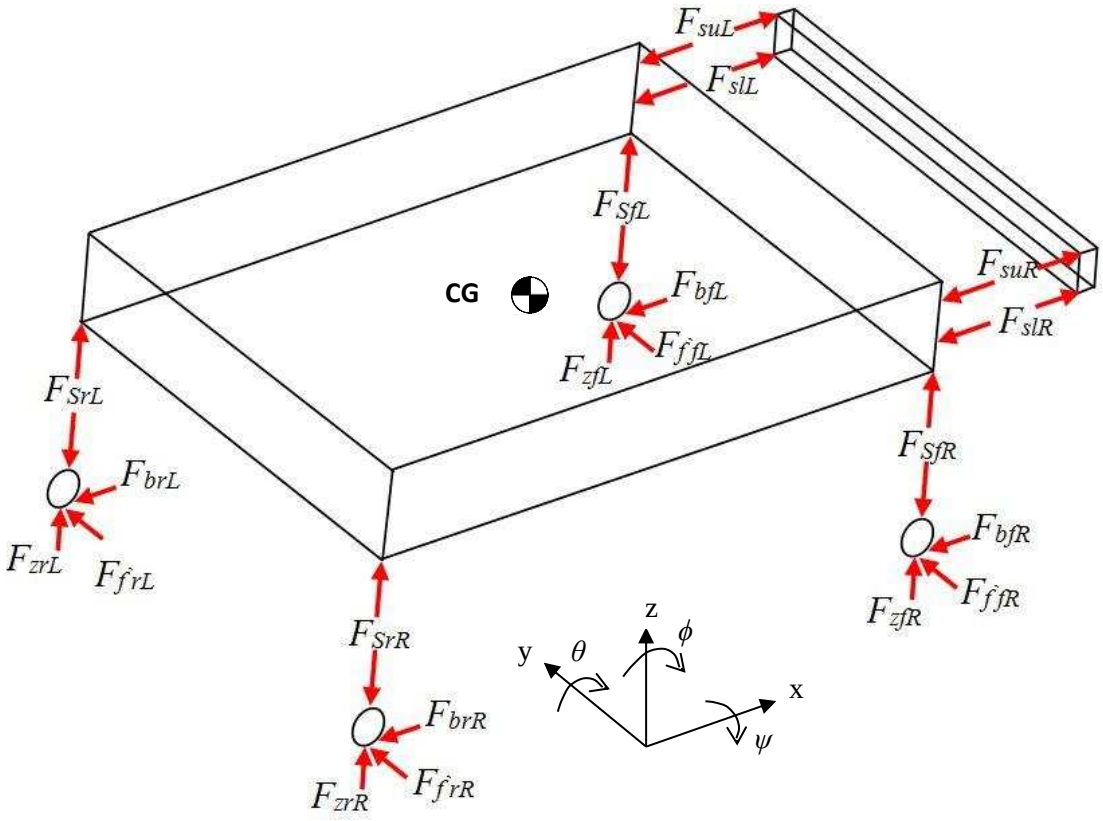

Figure 2: Free body diagram of the mathematical model

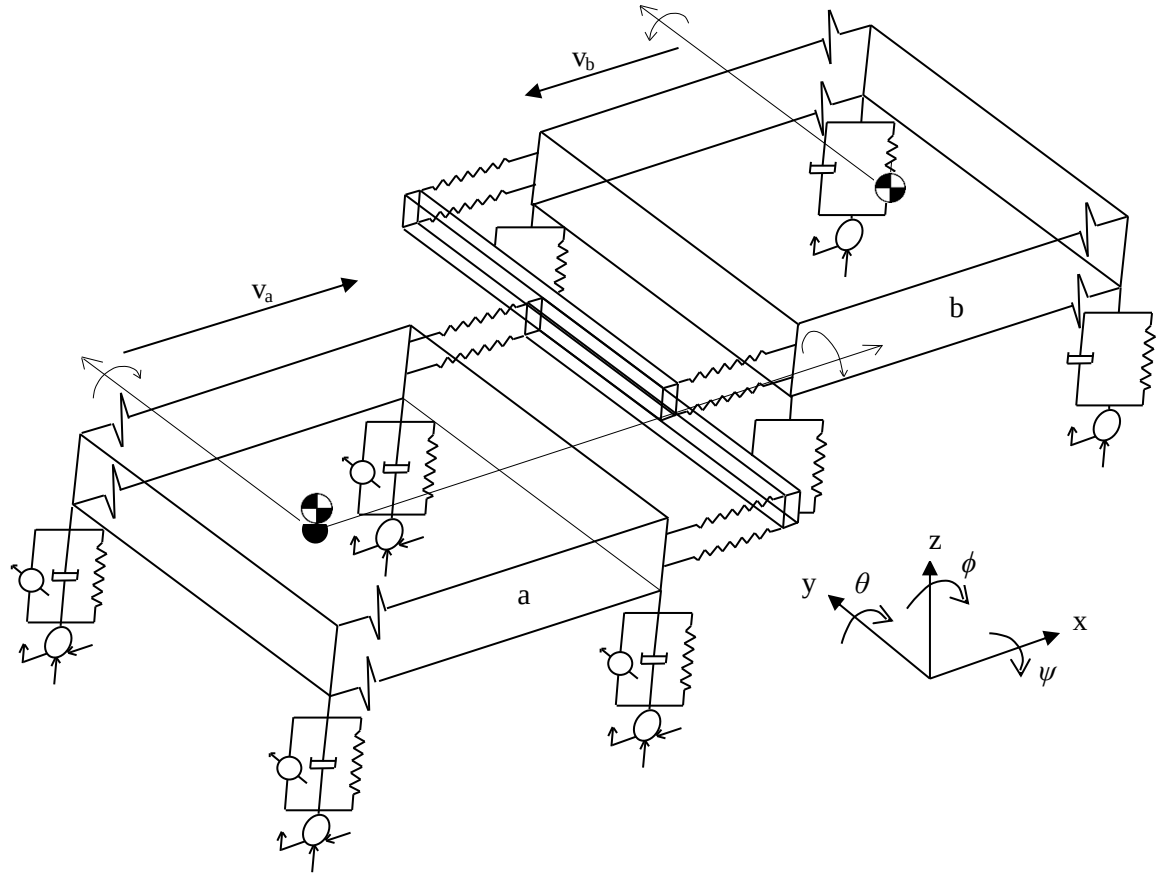

Figure 3 (a): Vehicle model before crash (offset frontal impact)

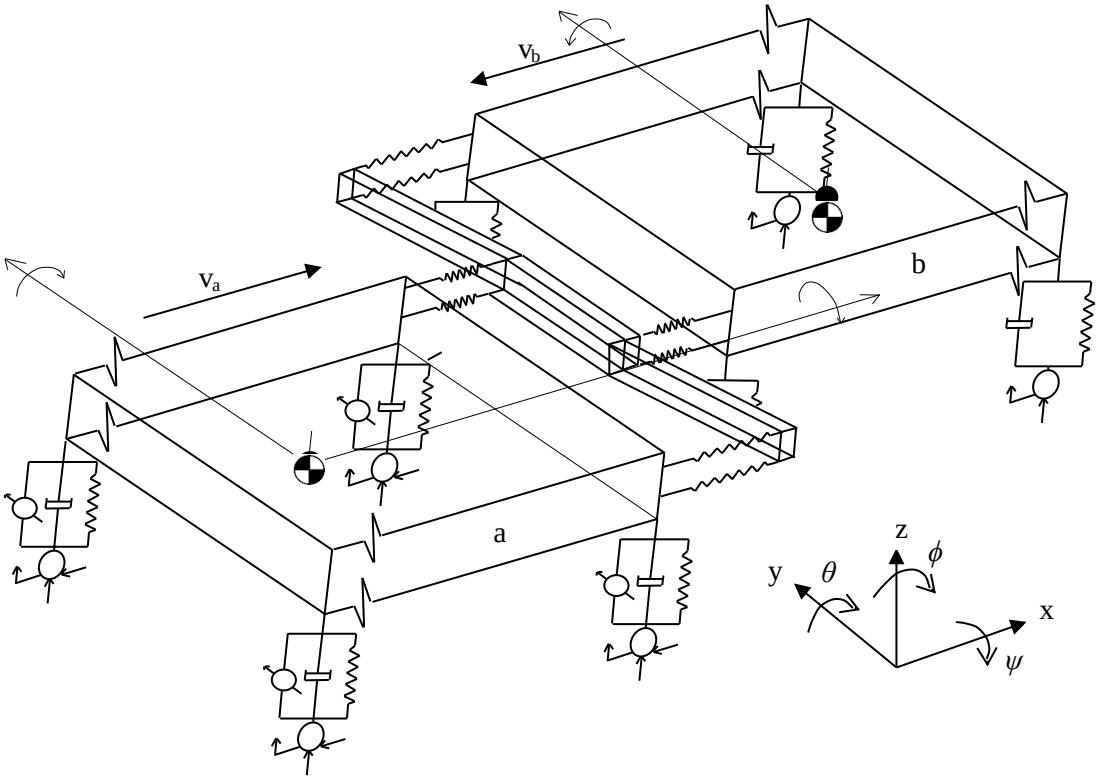

Figure 3 (b): Vehicle model after crash (offset frontal impact)

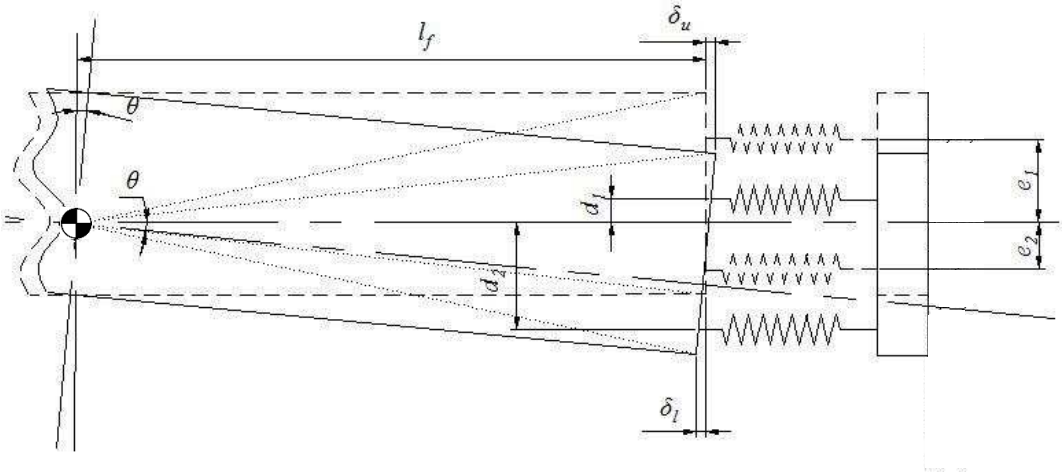

Figure 4: Illustration drawing of the front-end deformation due to vehicle pitching

(---- Before pitching —— After pitching)

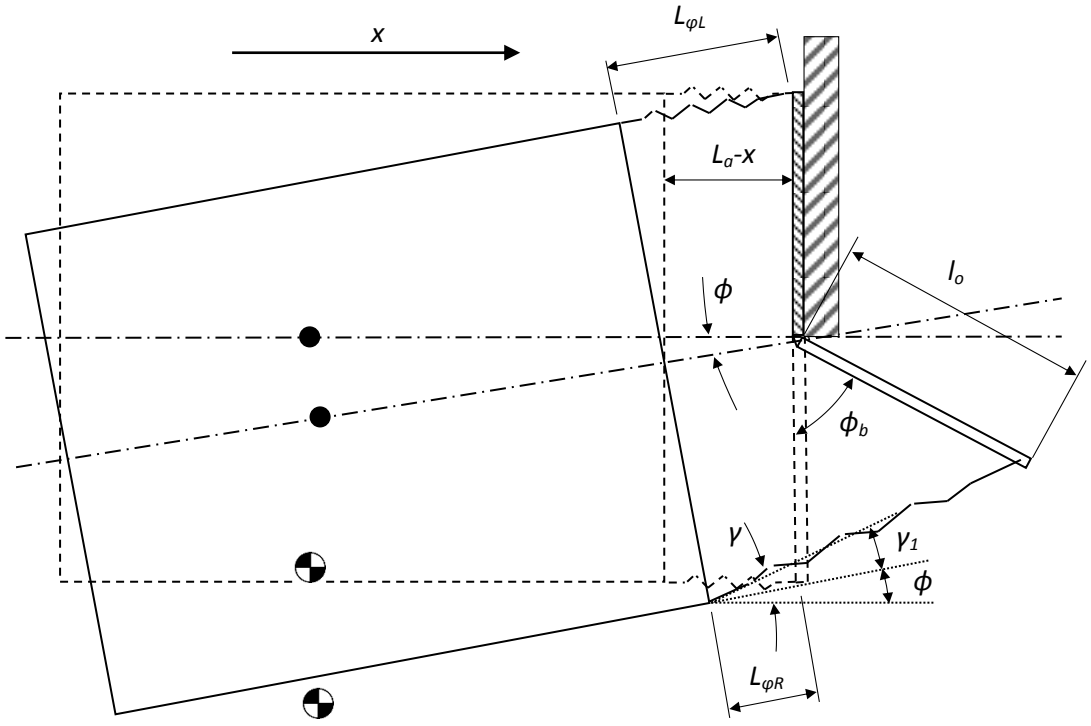

Figure 5: Illustration drawing of the front-end deformation due to vehicle yawing

- - (- Before yawing —After yawing)

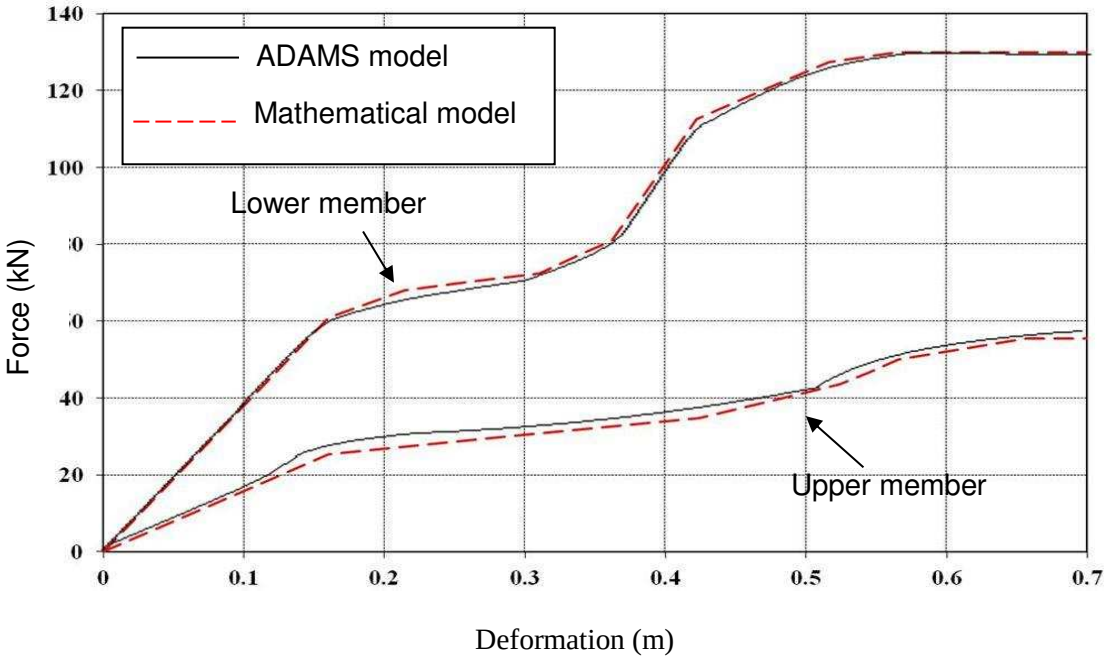

Figure 6: Force deformation characteristics for upper and lower rails

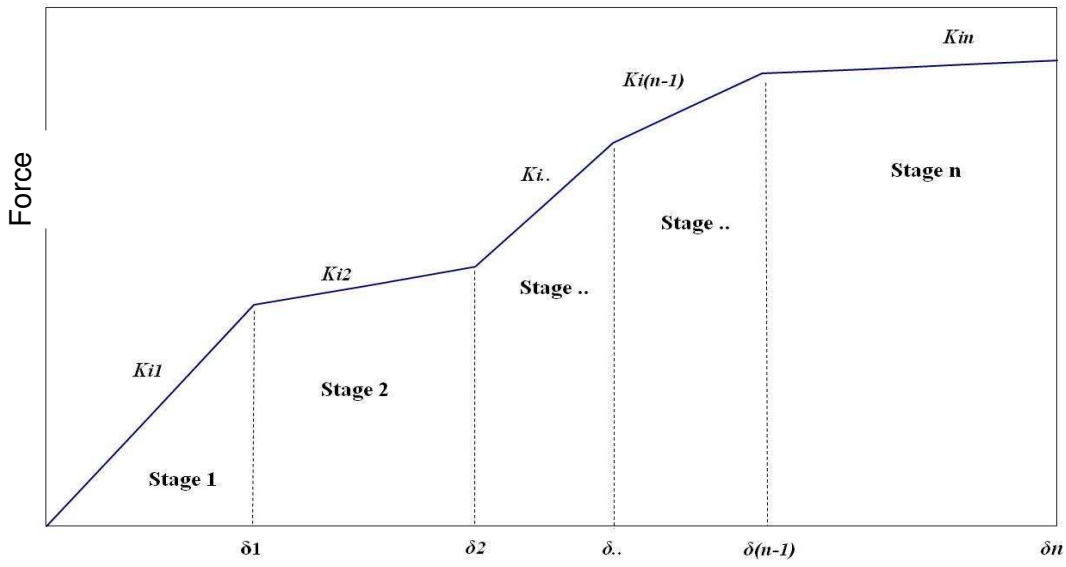

Figure 7: General piecewise force-deformation characteristics

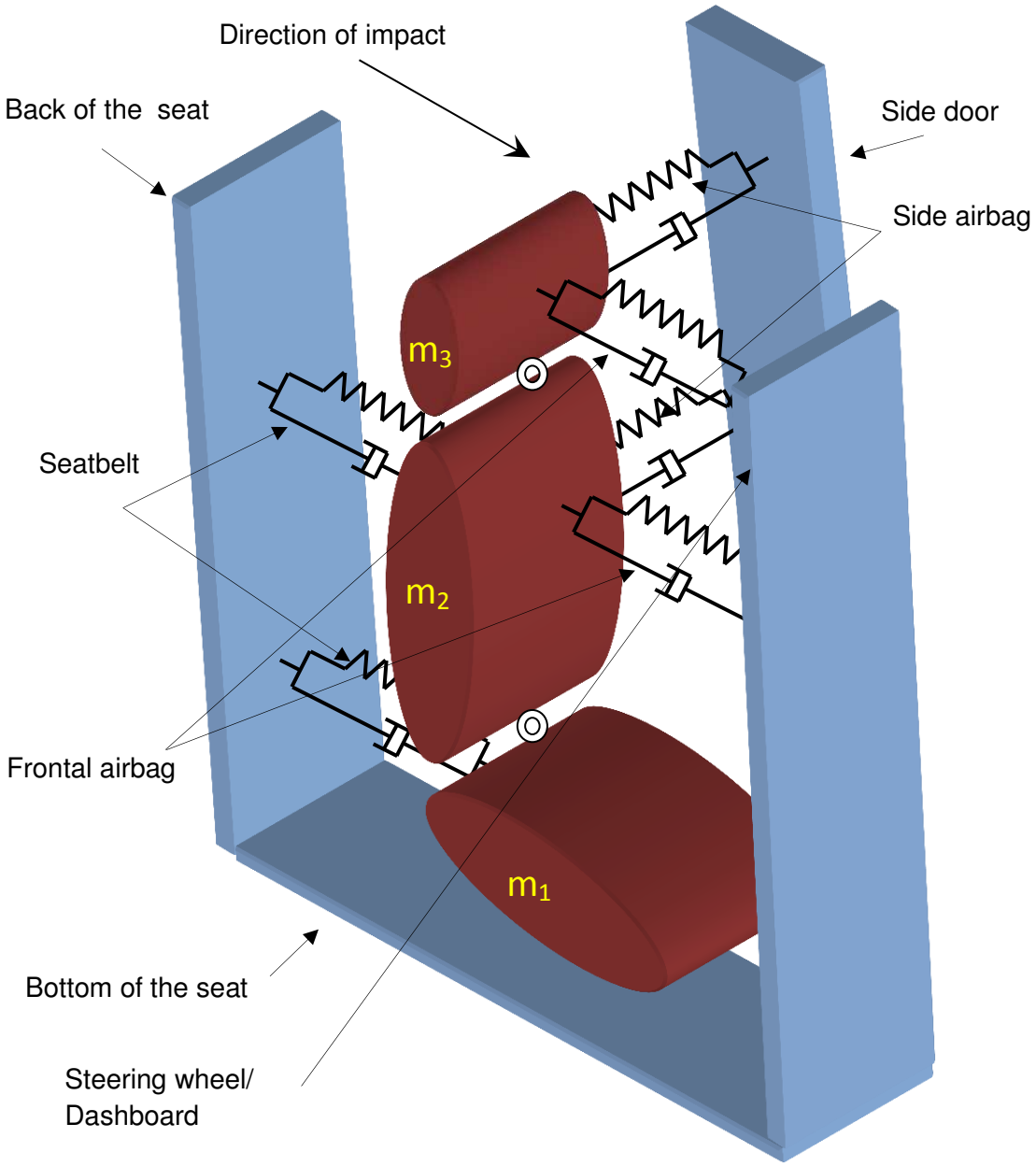

Figure 8: Multi-body occupant model

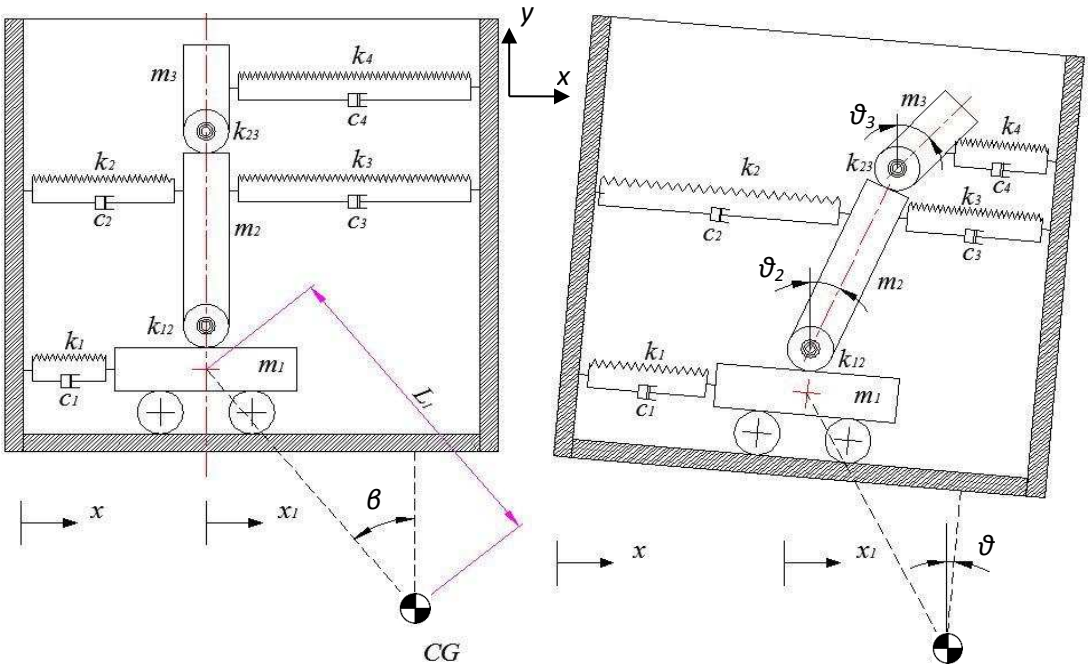

Figure 9 (a): Side view of the occupant model

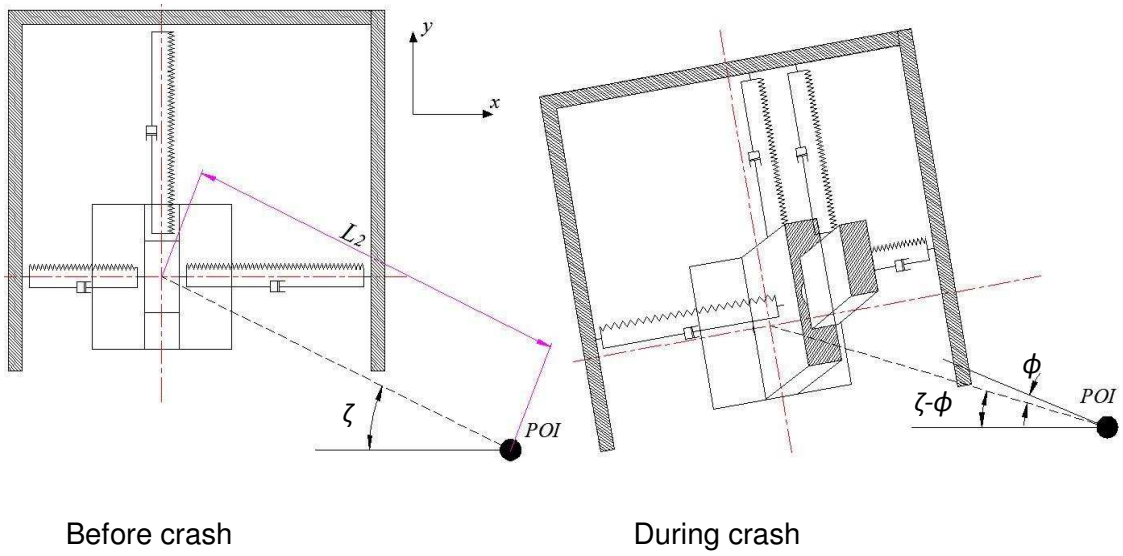

Figure 9 (b): Top view of the occupant model (POI: Point of Impact)

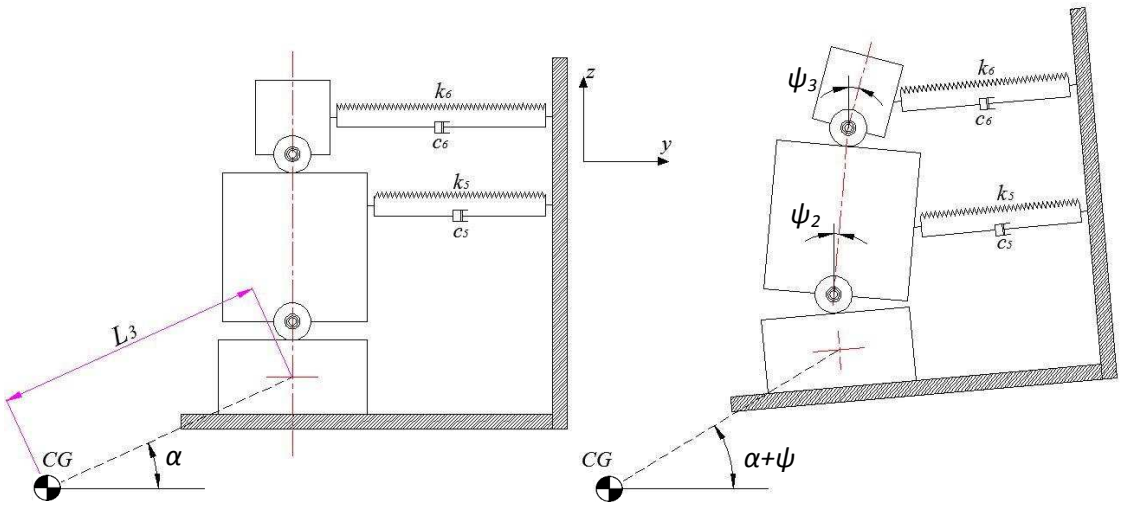

Figure 9 (c): Frontal view of the occupant model

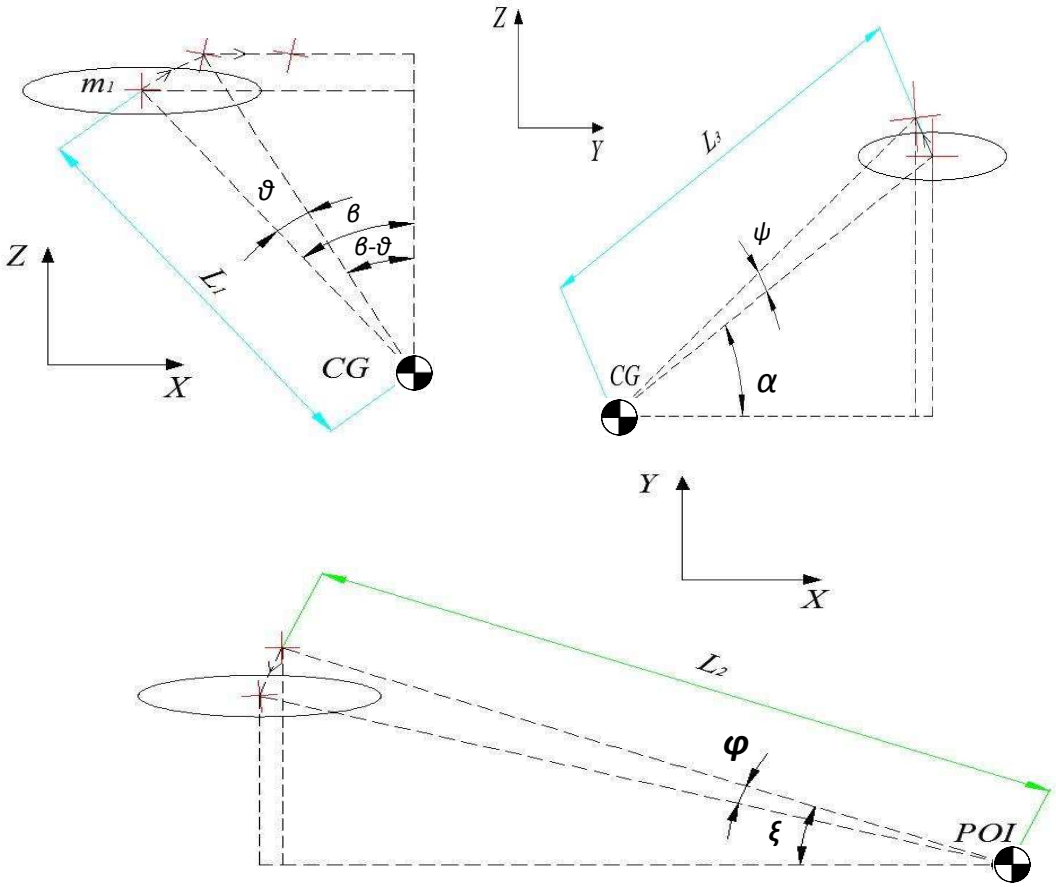

Figure 10: A schematic diagram of the occupant's lower body movement during impact

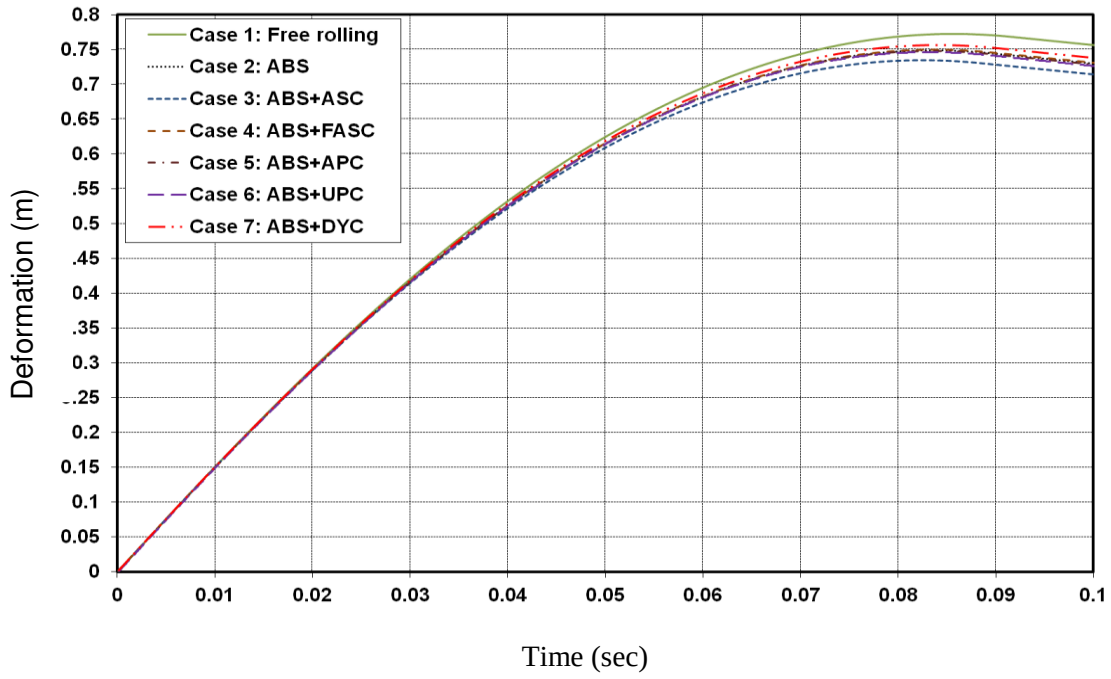

Figure 11: Deformation of the front-end structure (Offset frontal vehicle-to-vehicle impact) vehicle (a)

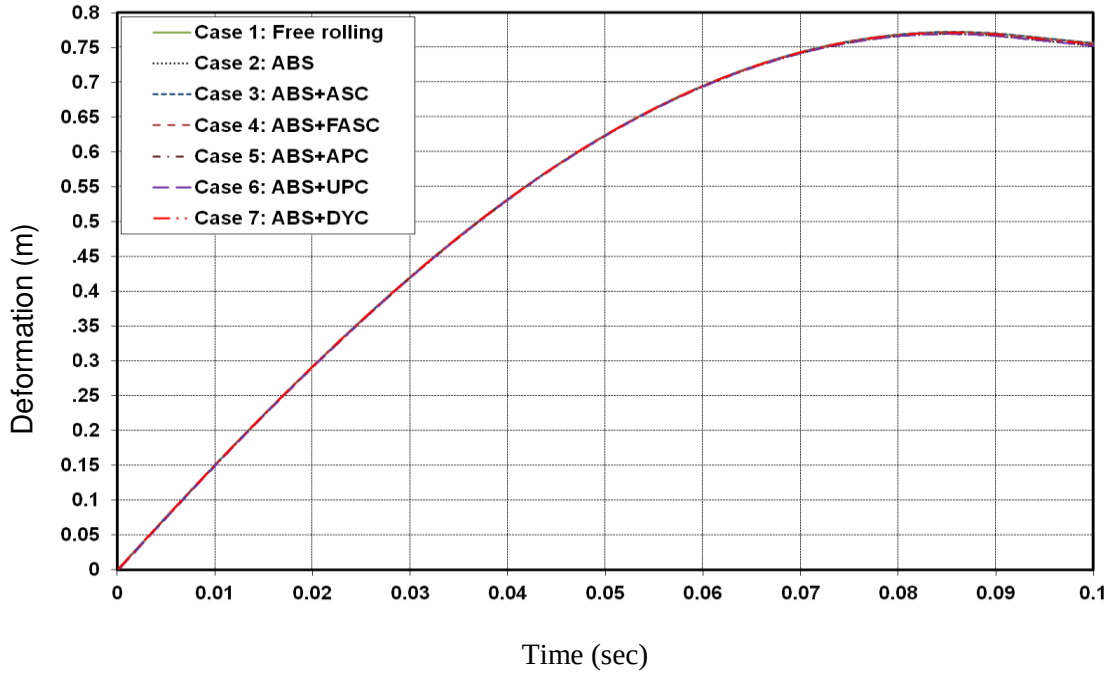

Figure 12: Deformation of the front-end structure (Offset frontal vehicle-to-vehicle impact), vehicle (b)

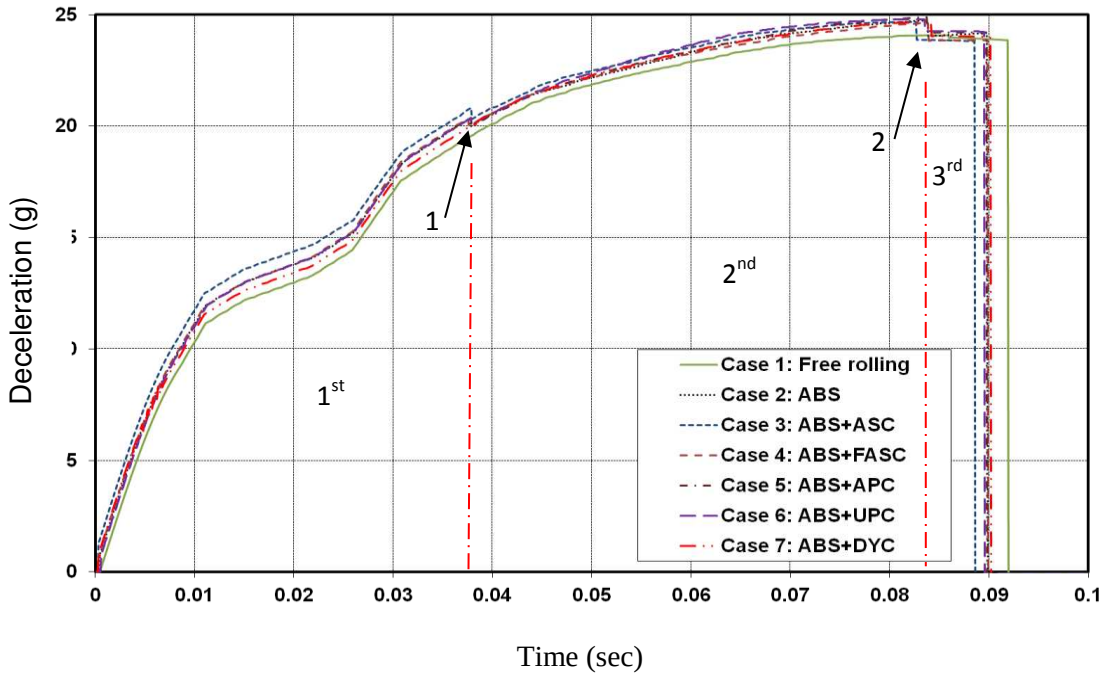

Figure 13: Vehicle body deceleration (Offset frontal vehicle-to-vehicle impact), vehicle (a)

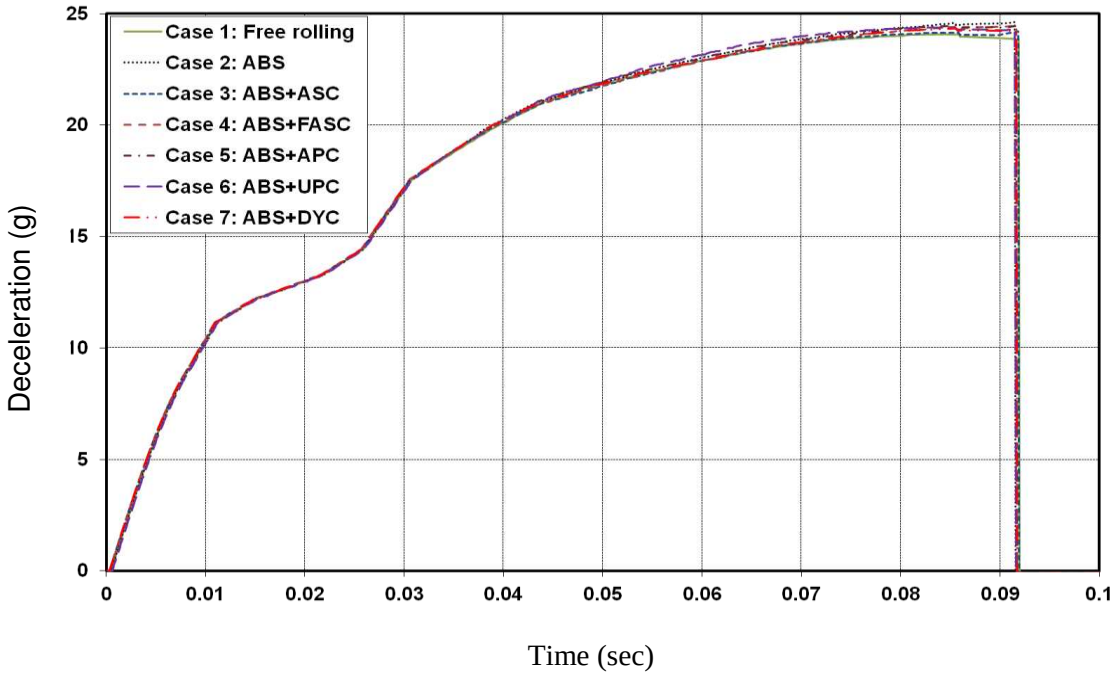

Figure 14: Vehicle body deceleration (Offset frontal vehicle-to-vehicle impact), vehicle (b)

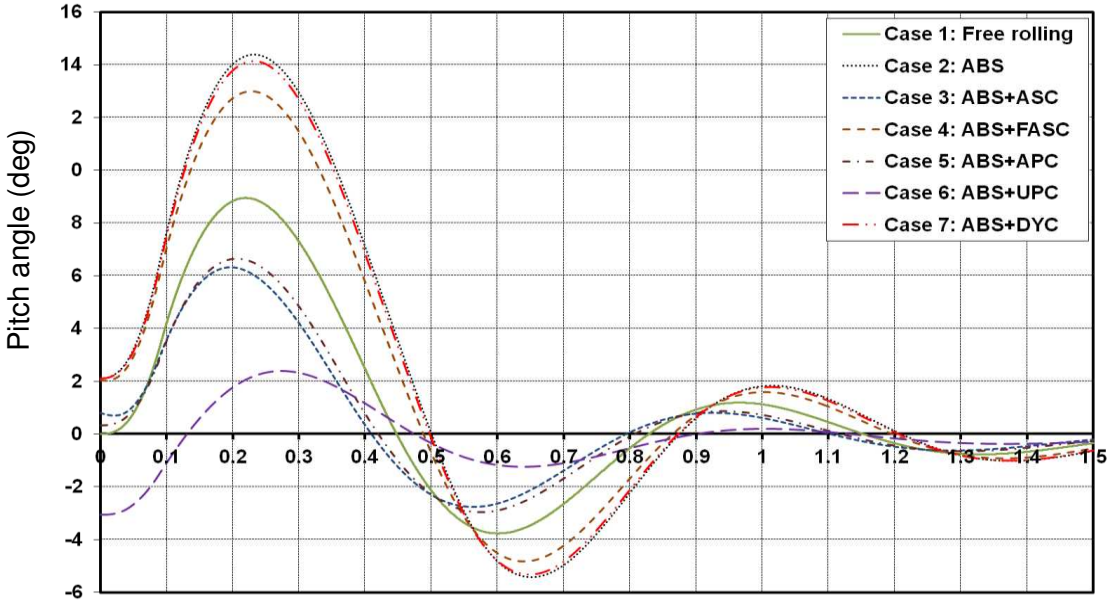

Figure 15: Vehicle body pitch angle (Offset frontal vehicle-to-vehicle impact), vehicle (a)

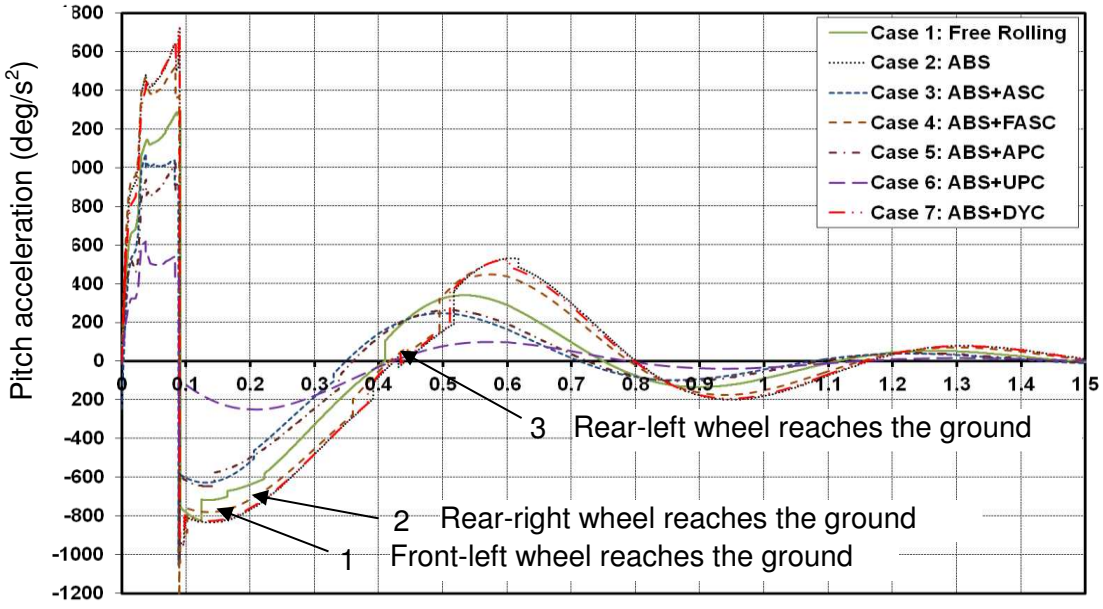

Figure 16: Vehicle body pitch acceleration (Offset frontal vehicle-to-vehicle impact), vehicle (a)

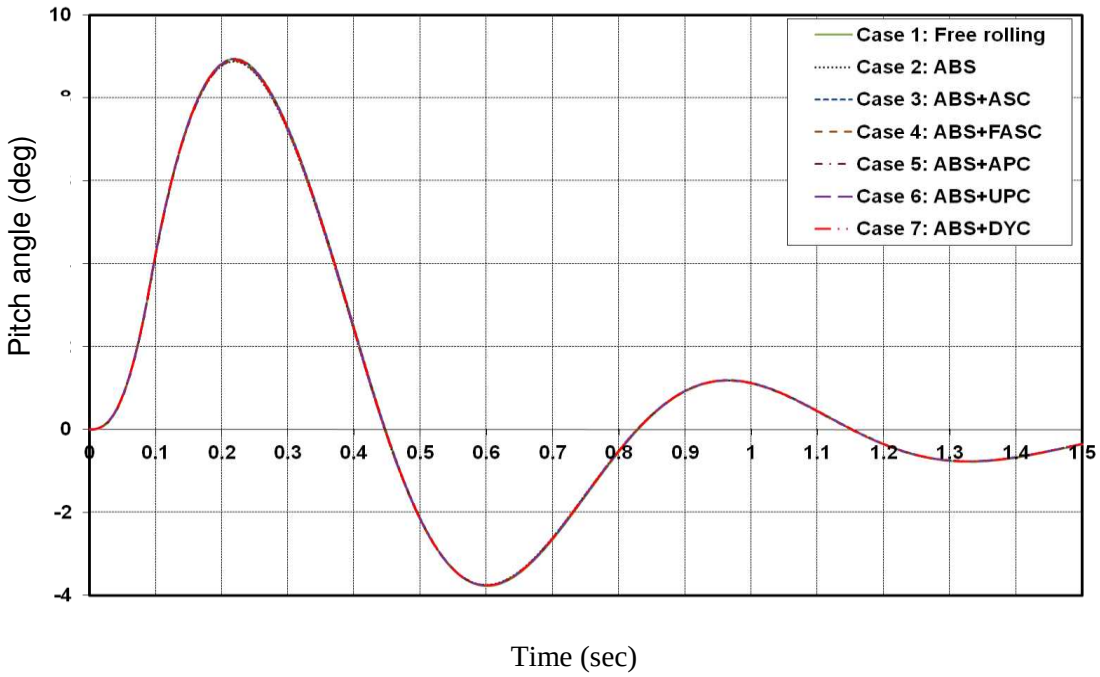

Figure 17: Vehicle body pitch angle (Offset frontal vehicle-to-vehicle impact), vehicle (b)

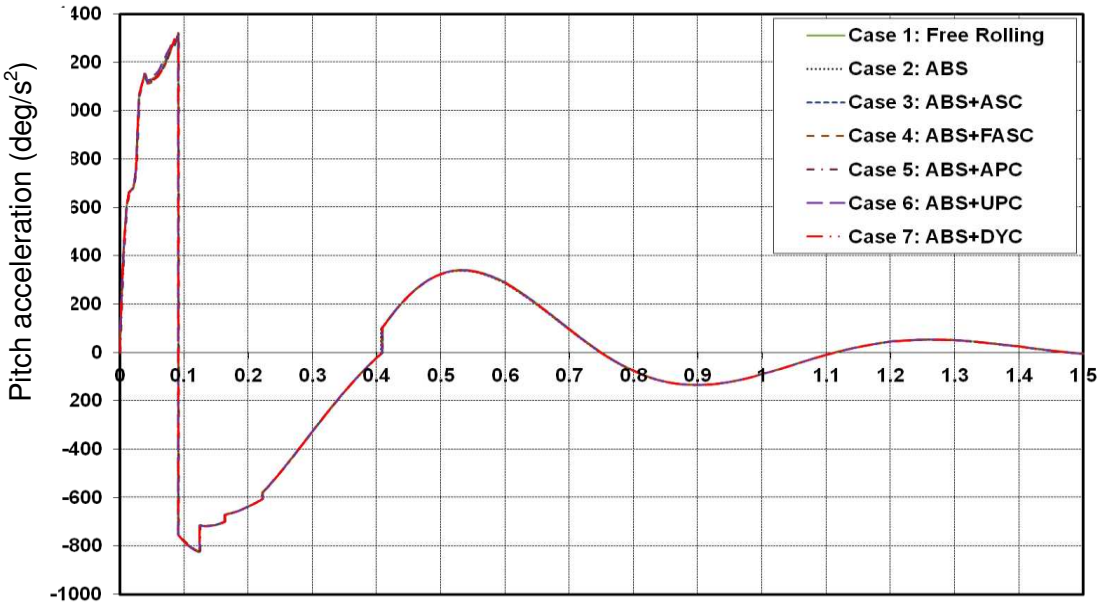

Figure 18: Vehicle body pitch acceleration (Offset frontal vehicle-to-vehicle impact), vehicle (b)

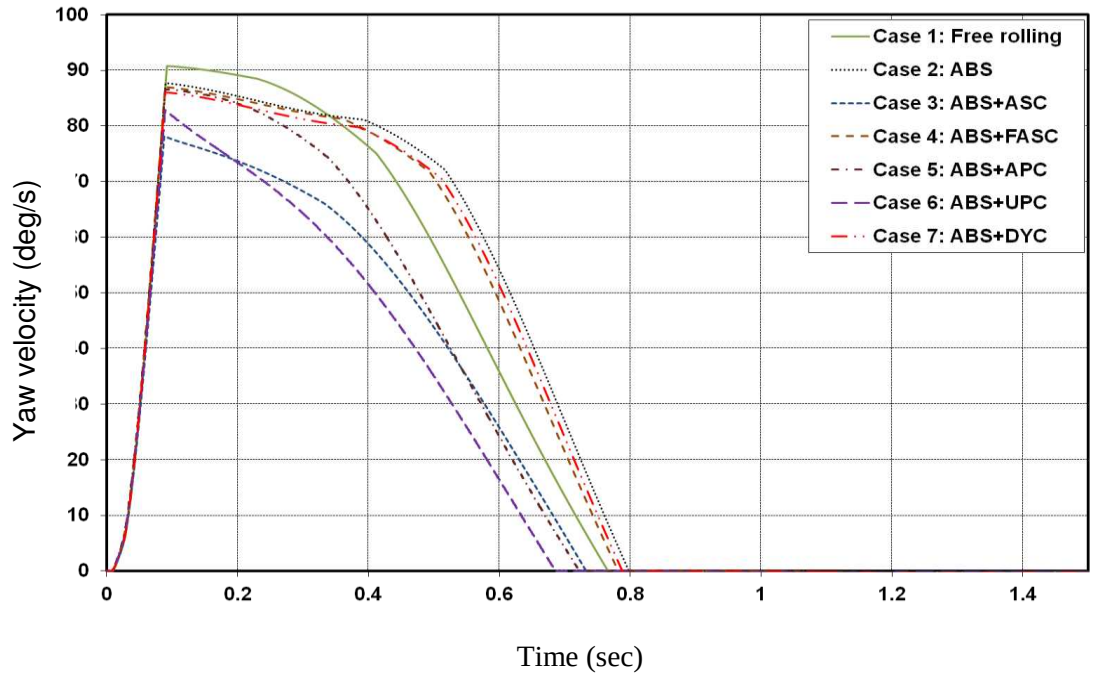

Figure 19: Vehicle body yaw velocity (Offset frontal vehicle-to-vehicle impact), vehicle (a)

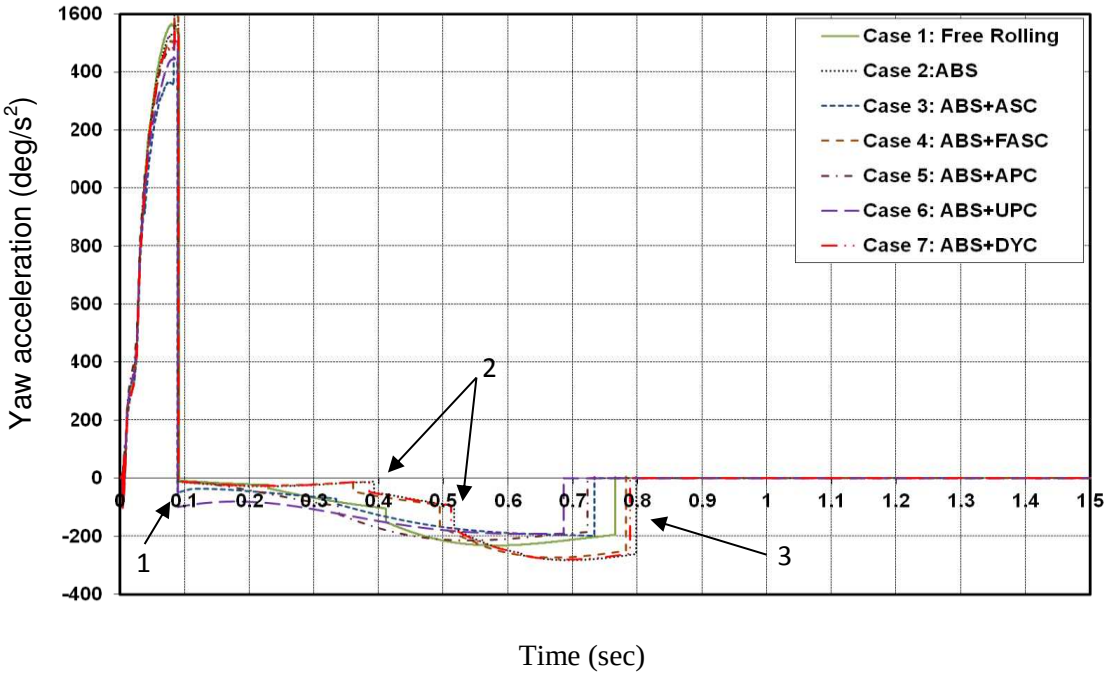

Figure 20: Vehicle body yaw acceleration (Offset frontal vehicle-to-vehicle impact), vehicle (a)

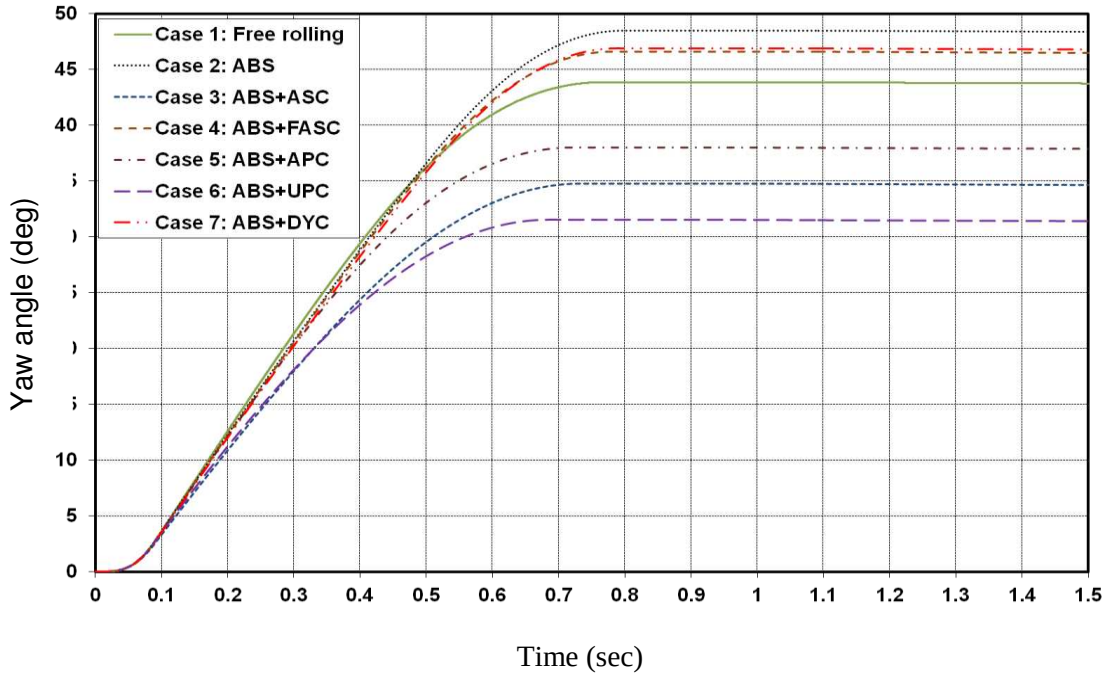

Figure 21: Vehicle body yaw angle (Offset frontal vehicle-to-vehicle impact), vehicle (a)

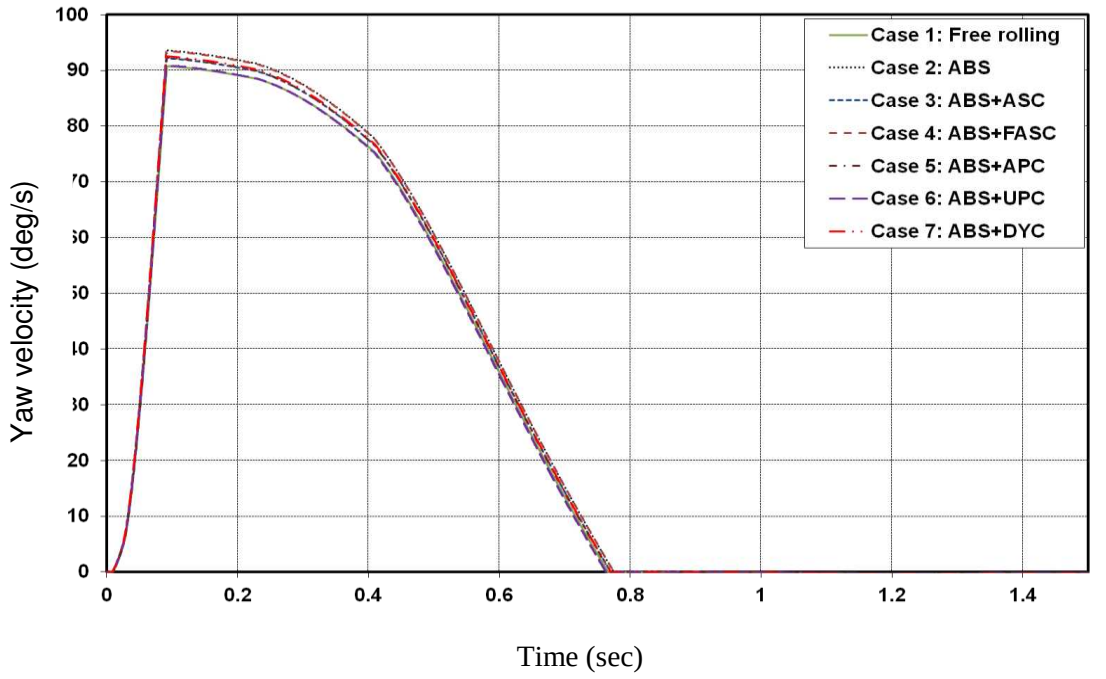

Figure 22: Vehicle body yaw velocity (Offset frontal vehicle-to-vehicle impact), vehicle (b)

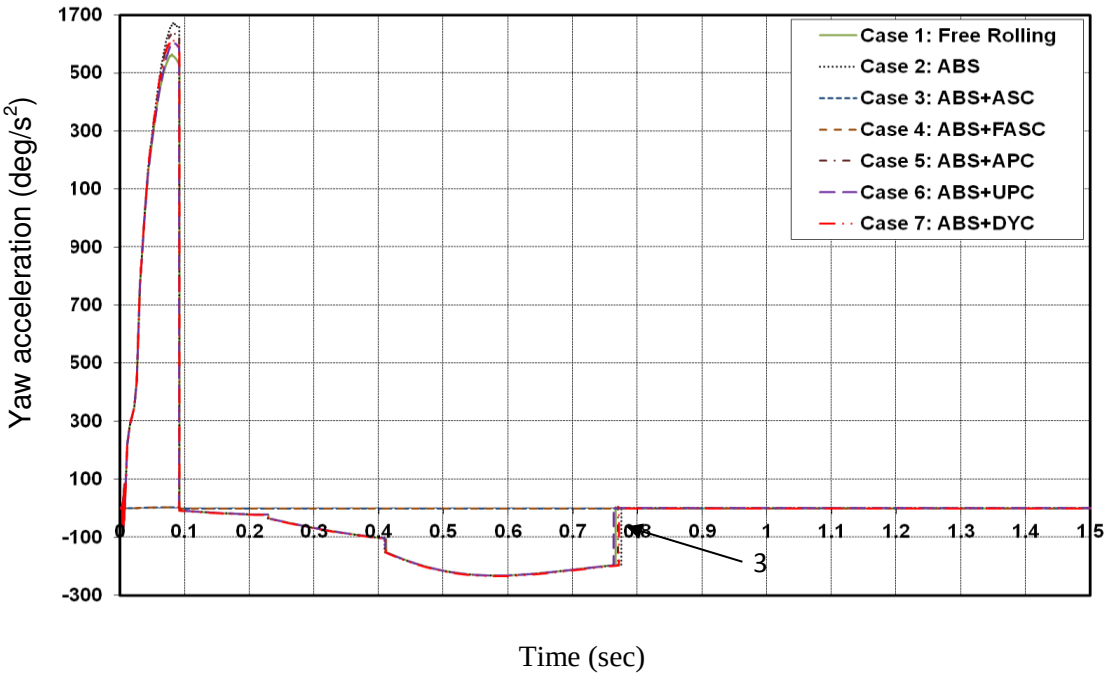

Figure 23: Vehicle body yaw acceleration (Offset frontal vehicle-to-vehicle impact), vehicle (b)

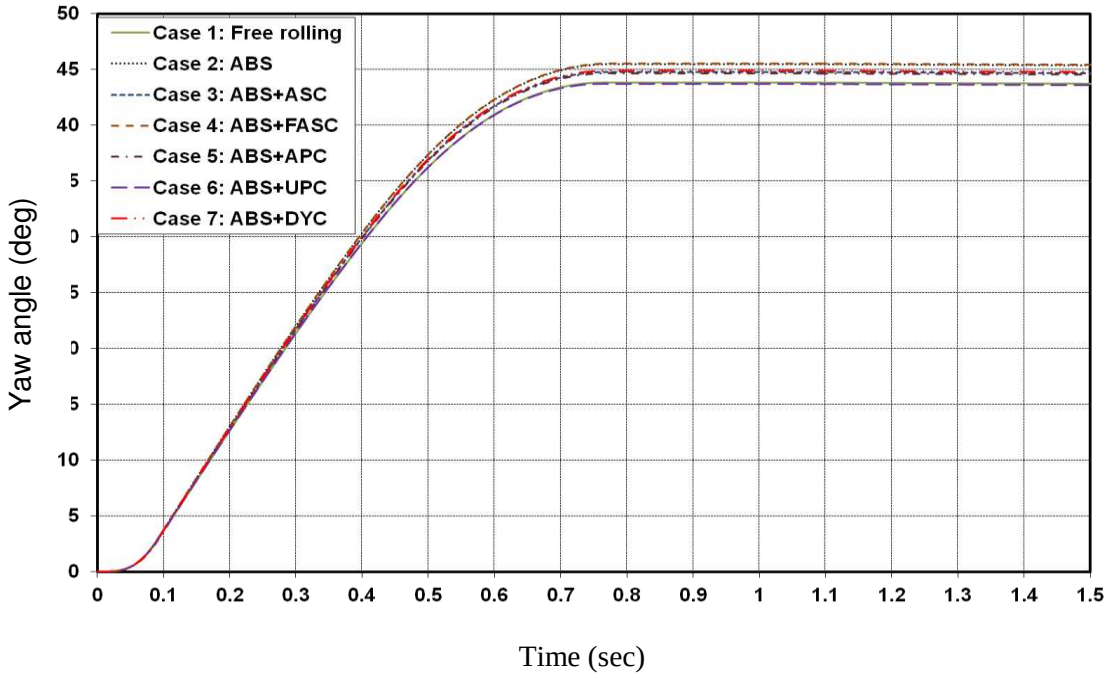

Figure 24: Vehicle body yaw angle (Offset frontal vehicle-to-vehicle impact), vehicle (b)

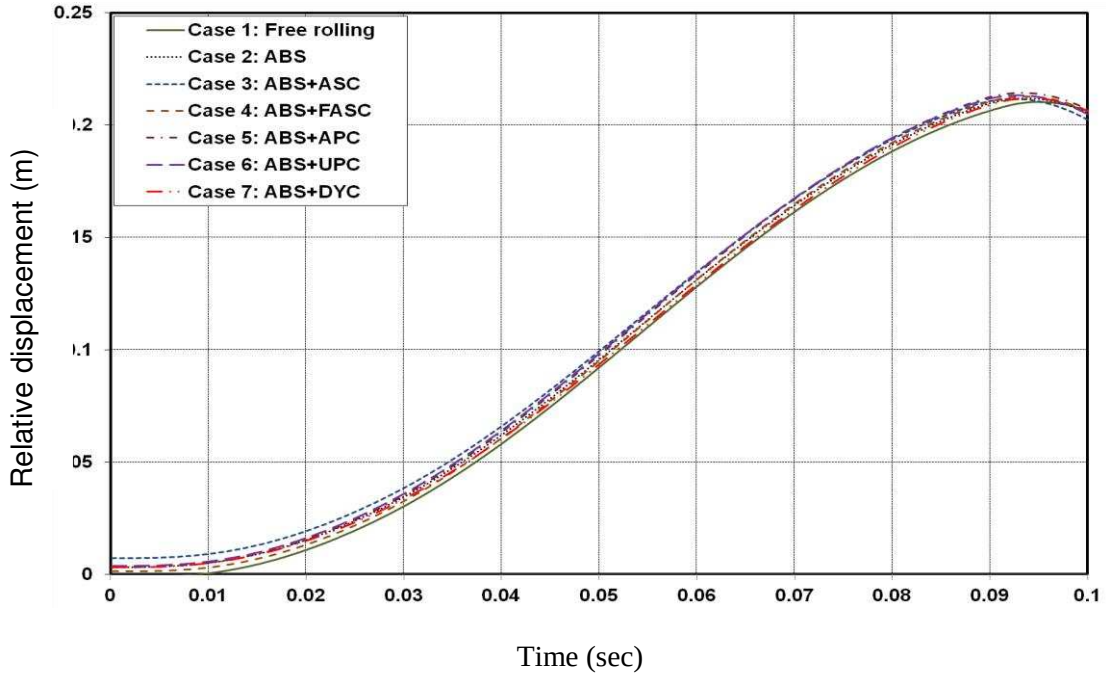

Figure 25: Occupant's pelvis displacement (Offset frontal vehicle-to-vehicle impact), vehicle (a)

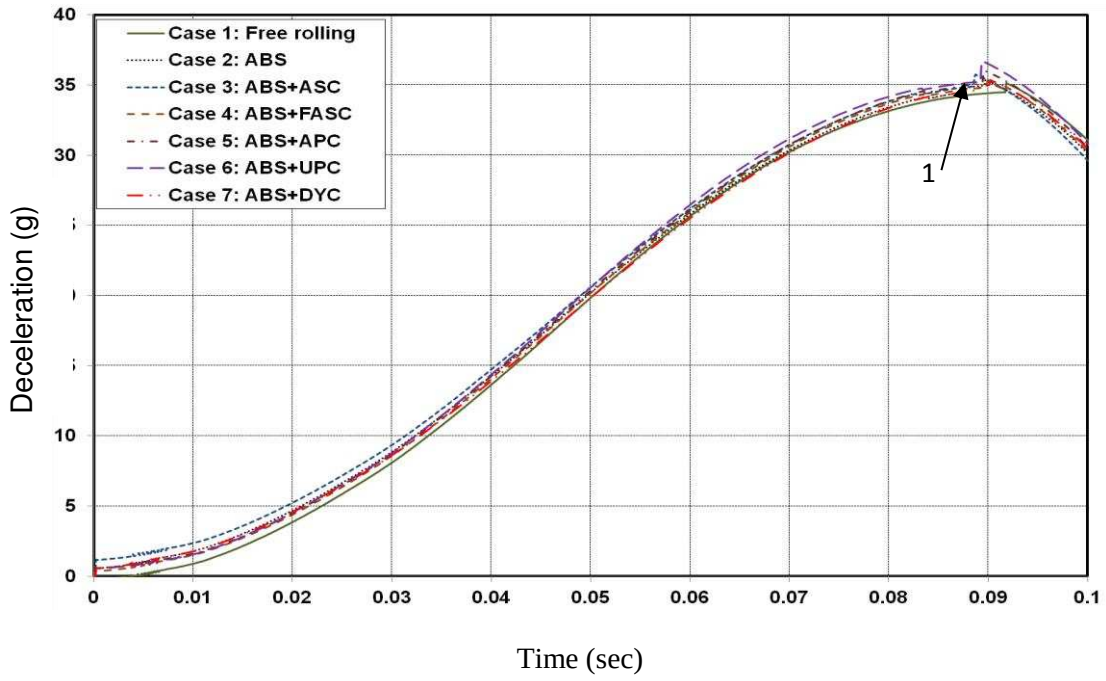

Figure 26: Occupant's pelvis deceleration (Offset frontal vehicle-to-vehicle impact), vehicle (a)

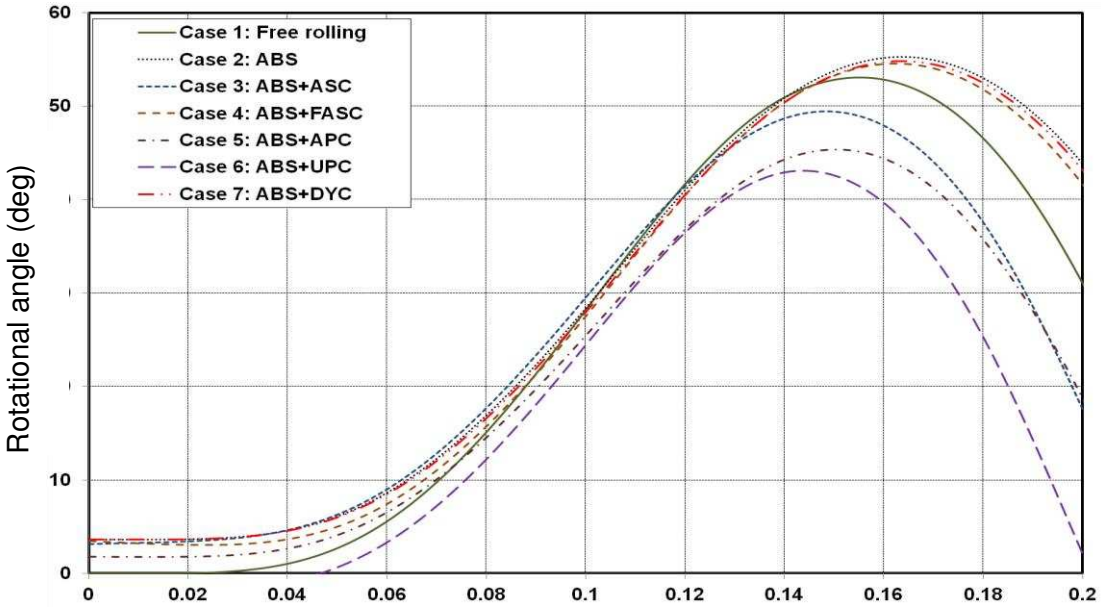

Figure 27: Rotational angle of the occupant's chest about y axis (Offset frontal vehicle-to-vehicle impact), vehicle (a)

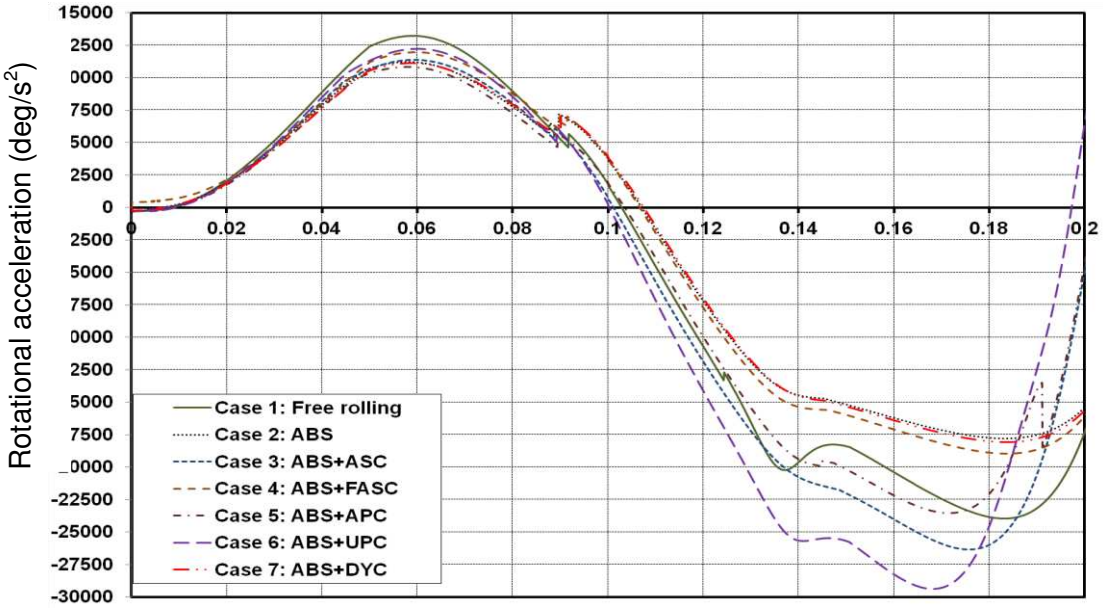

Figure 28: Rotational acceleration of the occupant's chest about y axis (Offset frontal vehicle-to-vehicle impact), vehicle (a)

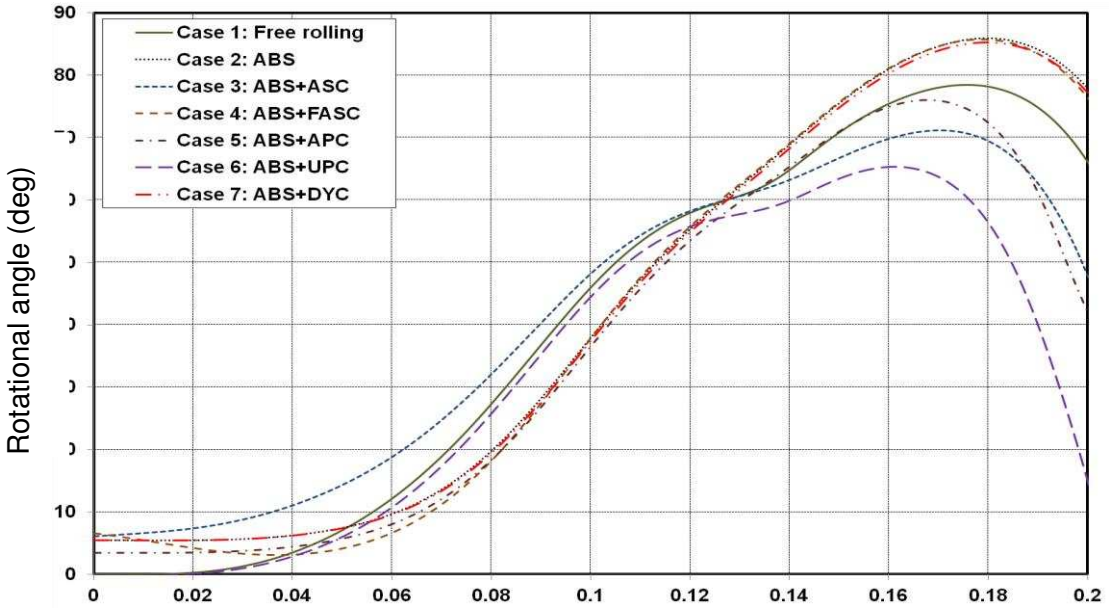

Figure 29: Rotational angle of the occupant's head about y axis (Offset frontal vehicle-to-vehicle impact), vehicle (a)

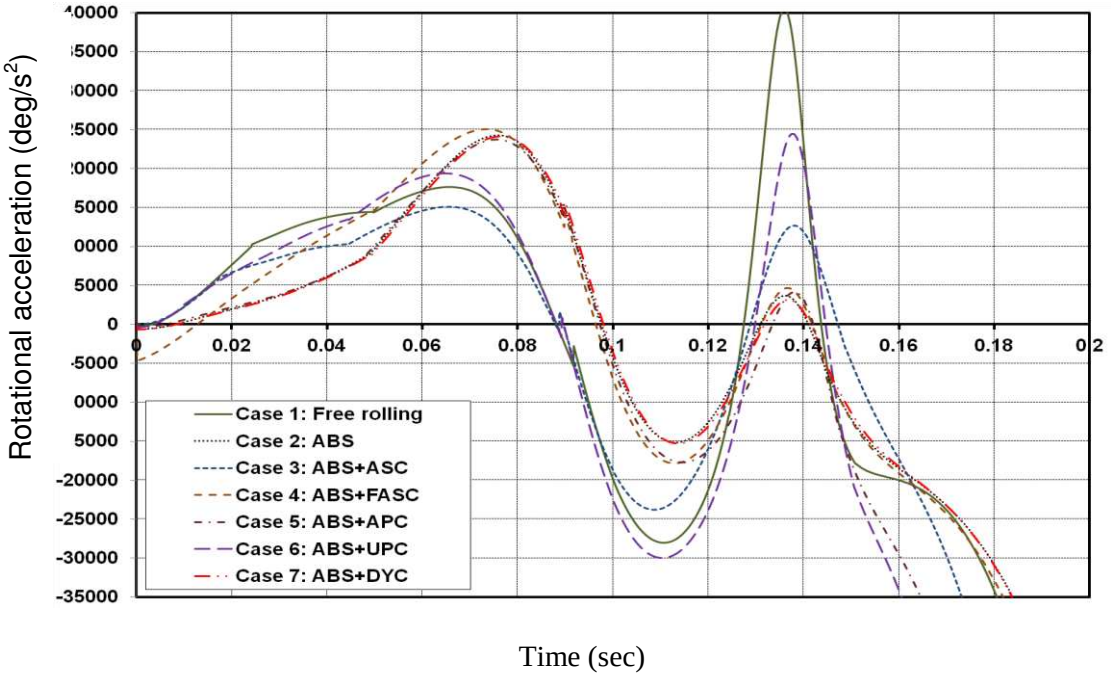

Figure 30: Rotational acceleration of the occupant's head about y axis (Offset frontal vehicle-to-vehicle impact), vehicle (a)

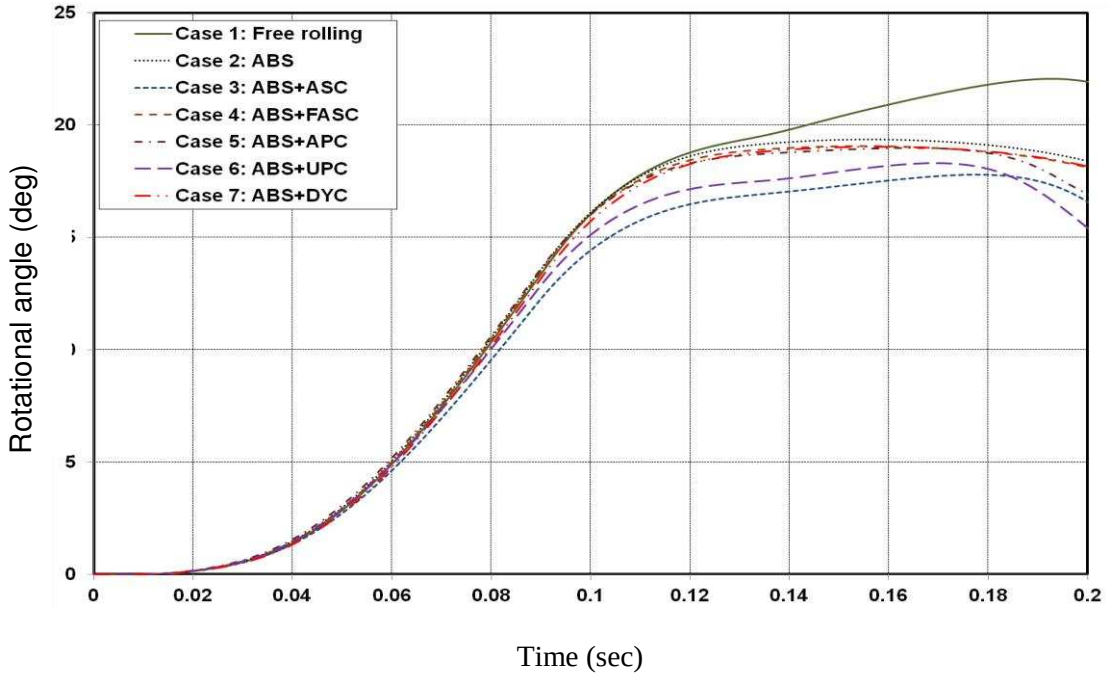

Figure 31: Rotational angle of the occupant's chest about x axis (Offset frontal vehicle-to-vehicle impact), vehicle (a)

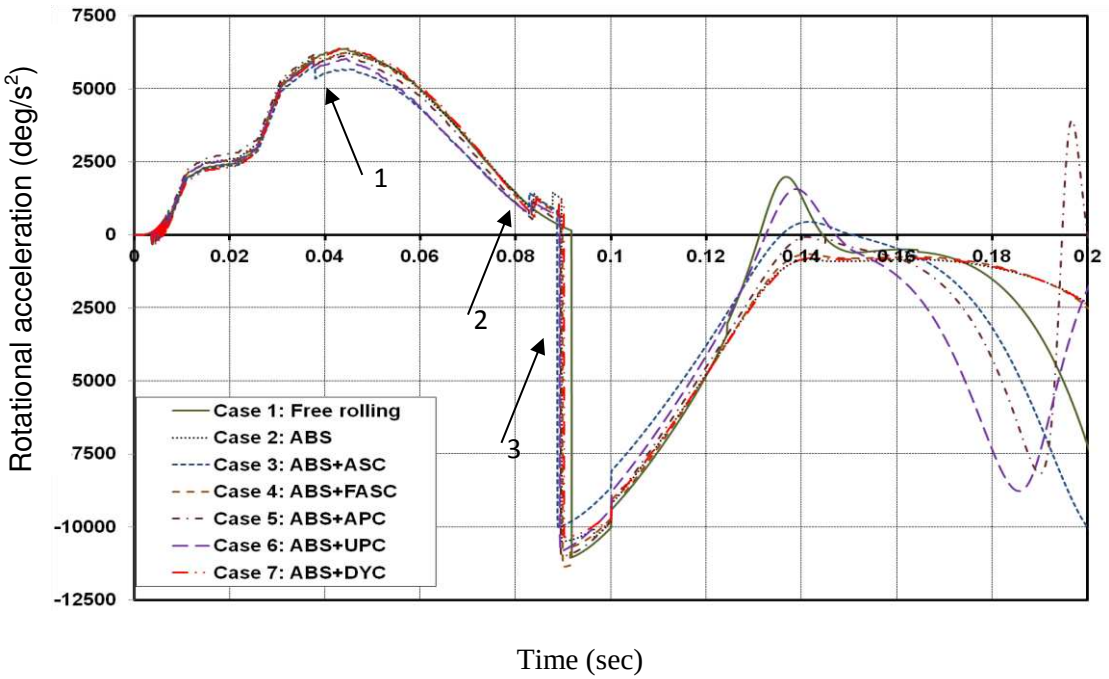

Figure 32: Rotational acceleration of the occupant's chest about x axis (Offset frontal vehicle-to-vehicle impact), vehicle (a)

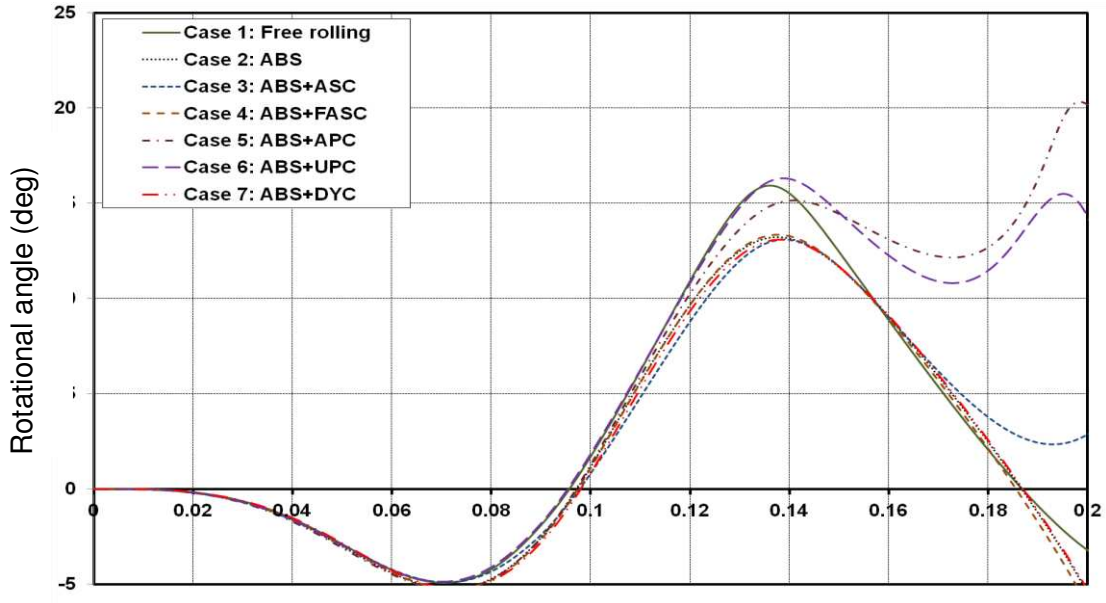

Figure 33: Rotational angle of the occupant's head about x axis (Offset frontal vehicle-to-vehicle impact), vehicle (a)

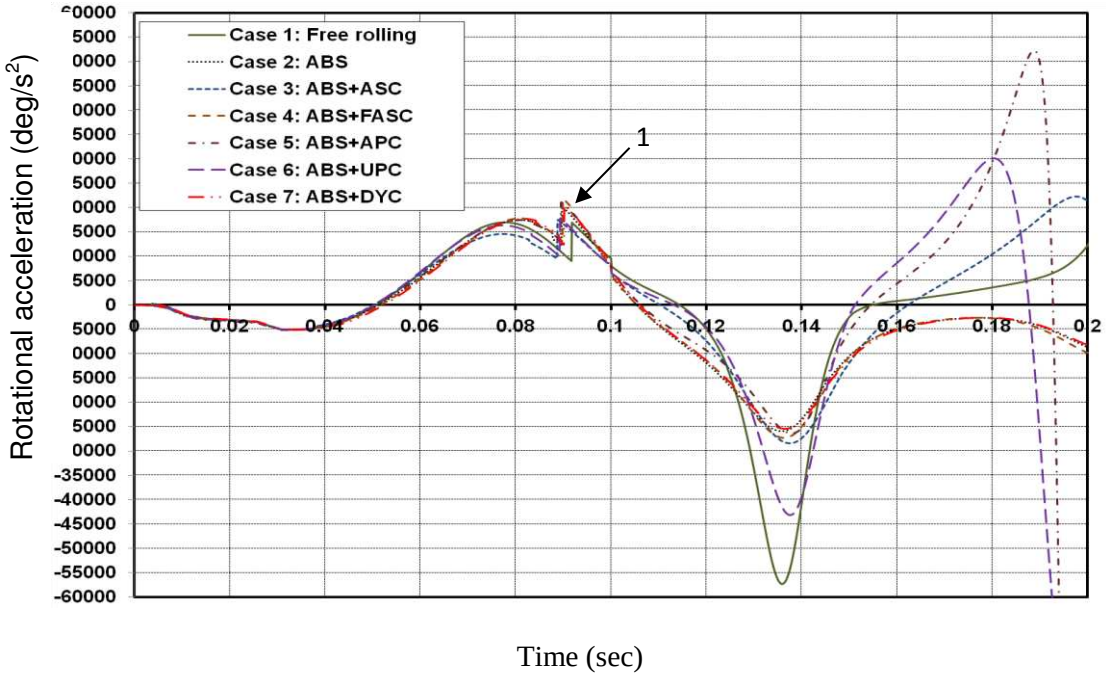

Figure 34: Rotational acceleration of the occupant's head about x axis (Offset frontal vehicle-to-vehicle impact), vehicle (a)

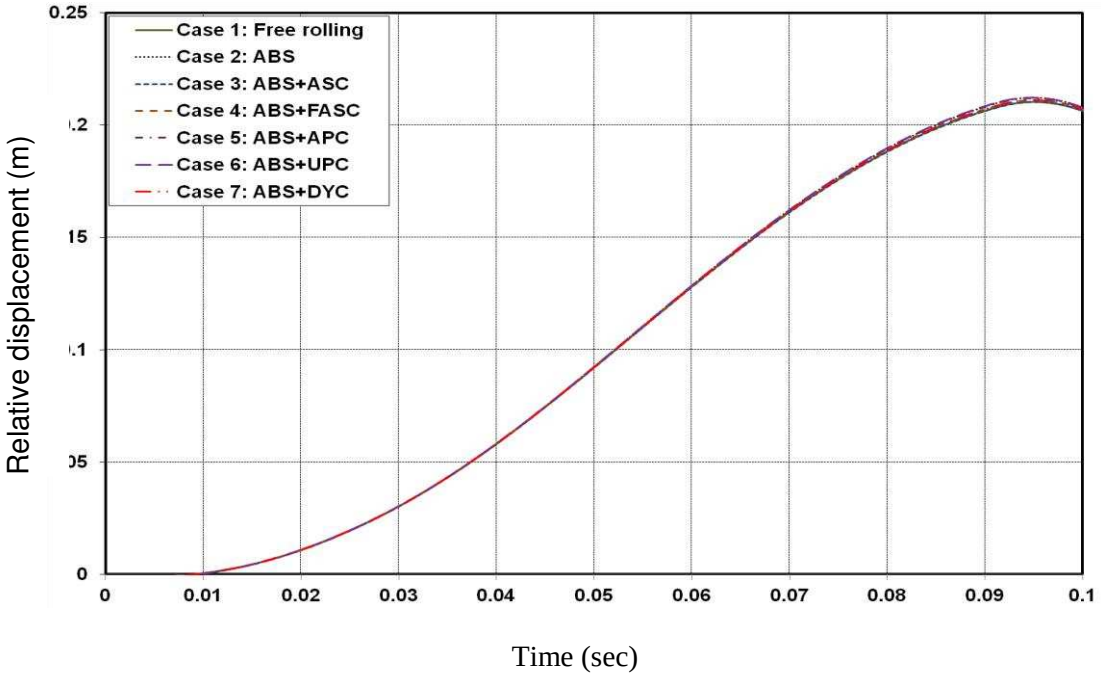

Figure 35: Occupant's pelvis displacement (Offset frontal vehicle-to-vehicle impact), vehicle (b)

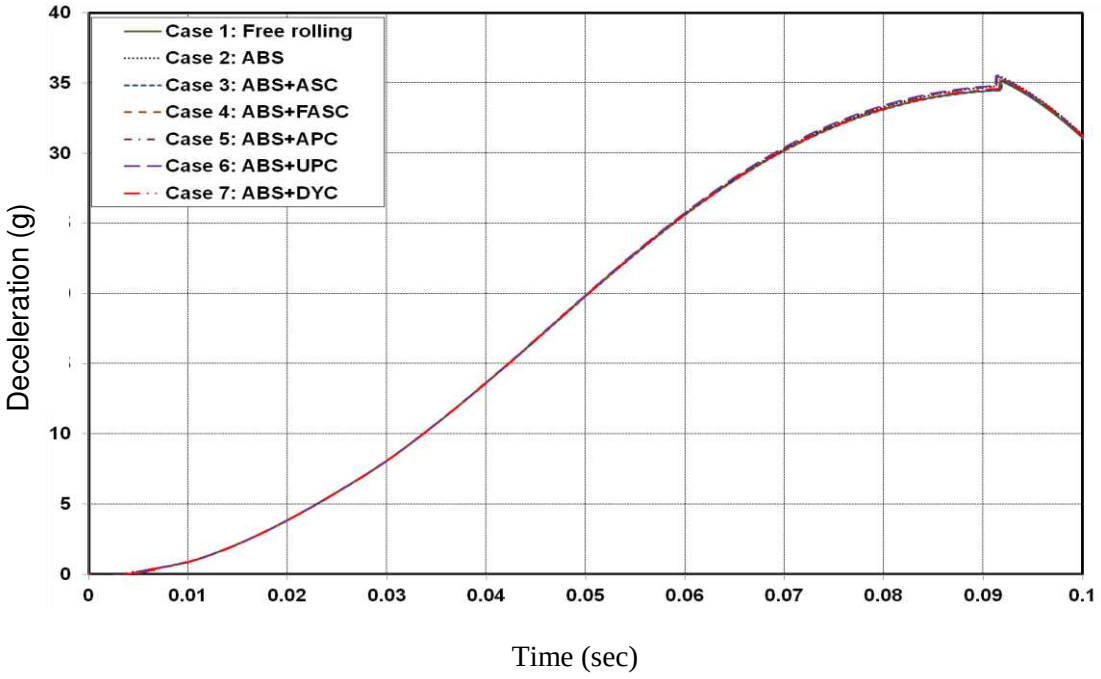

Figure 36: Occupant's pelvis deceleration (Offset frontal vehicle-to-vehicle impact), vehicle (b)

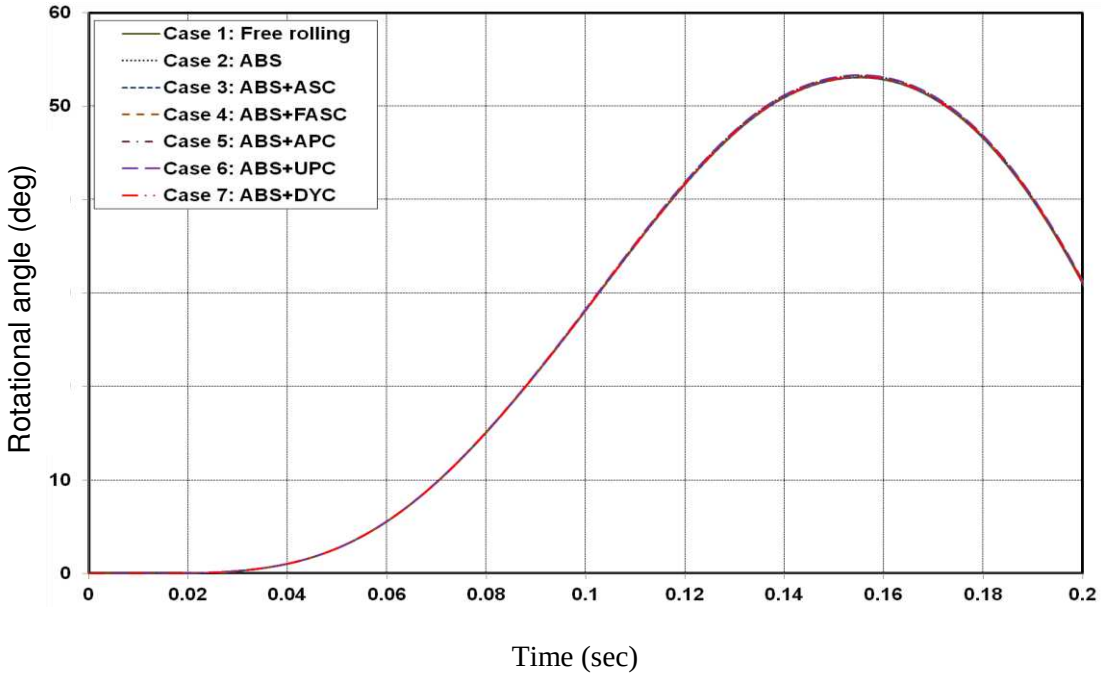

Figure 37: Rotational angle of the occupant's chest about y axis (Offset frontal vehicle-to-vehicle impact), vehicle (b)

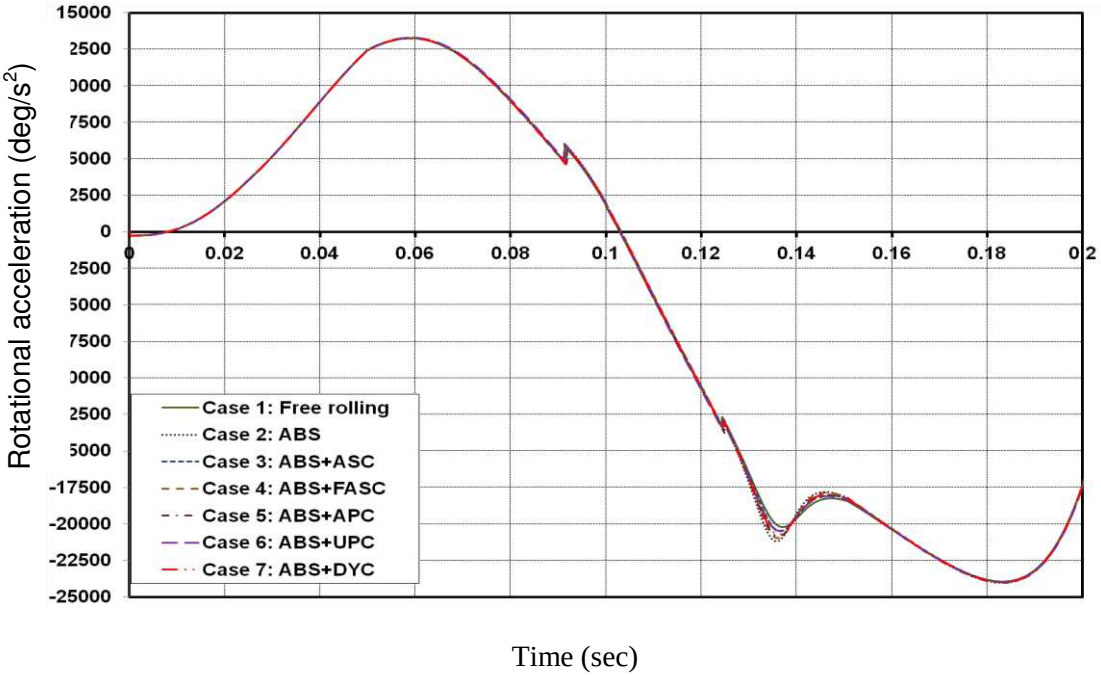

Figure 38: Rotational acceleration of the occupant's chest about y axis (Offset frontal vehicle-to-vehicle impact), vehicle (b)

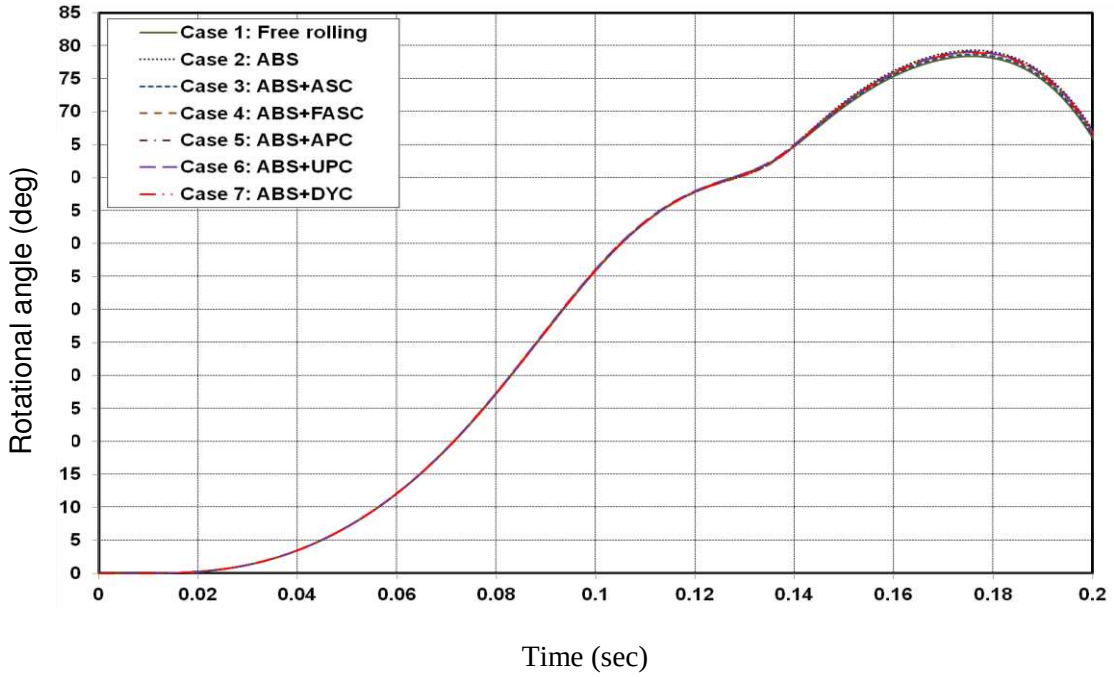

Figure 39: Rotational angle of the occupant's head about y axis (Offset frontal vehicle-to-vehicle impact), vehicle (b)

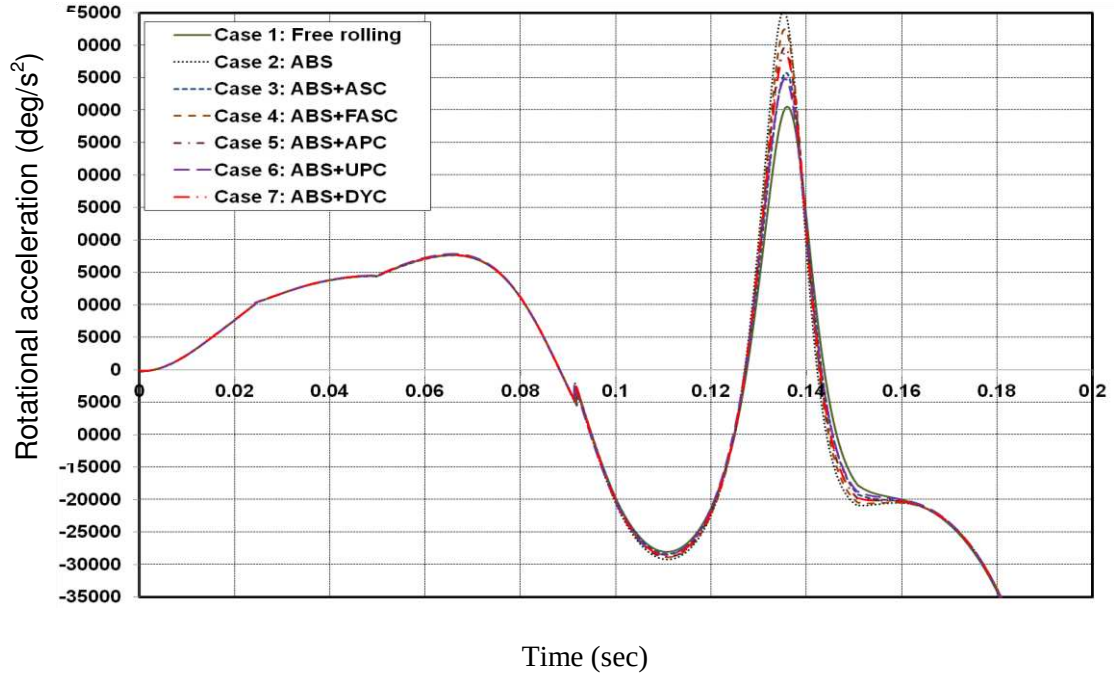

Figure 40: Rotational acceleration of the occupant's head about y axis (vehi Offset frontal vehicle-to-vehicle impact), vehicle (b)

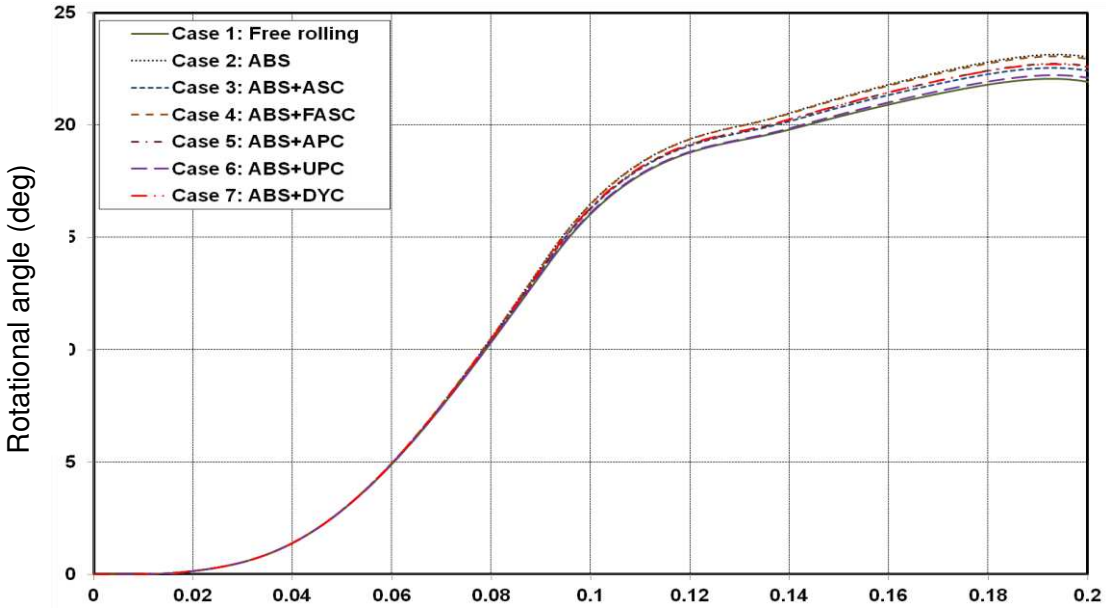

Figure 41: Rotational angle of the occupant's chest about x axis (Offset frontal vehicle-to-vehicle impact), vehicle (b)

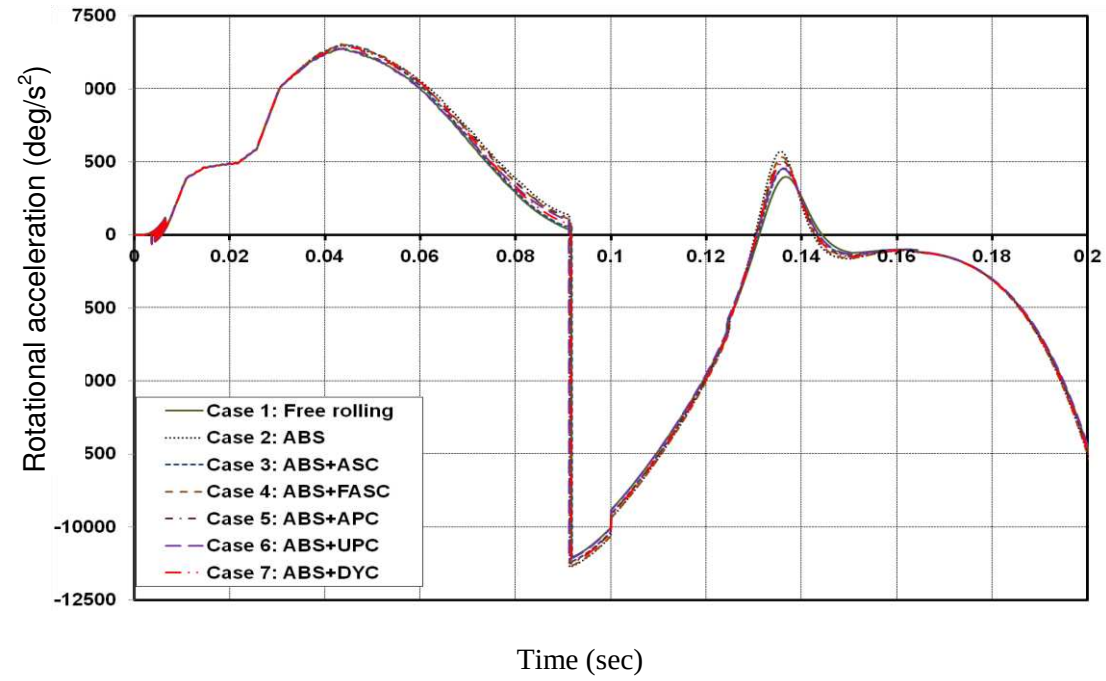

Figure 42: Rotational acceleration of the occupant's chest about x axis (Offset frontal vehicle-to-vehicle impact), vehicle (b)

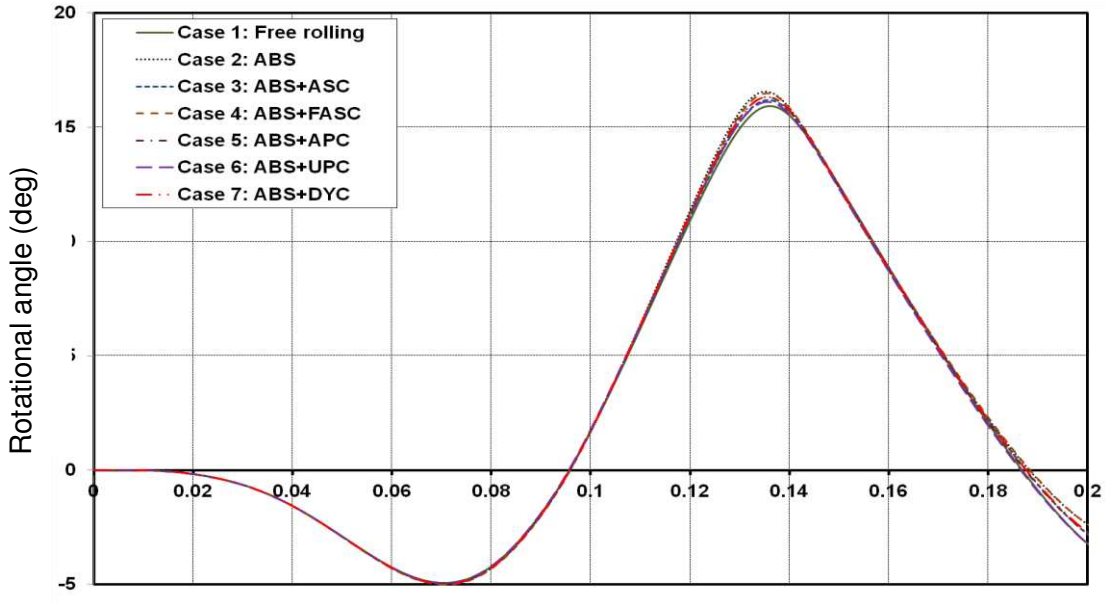

Figure 43: Rotational angle of the occupant's head about x axis (Offset frontal vehicle-to-vehicle impact), vehicle (b)

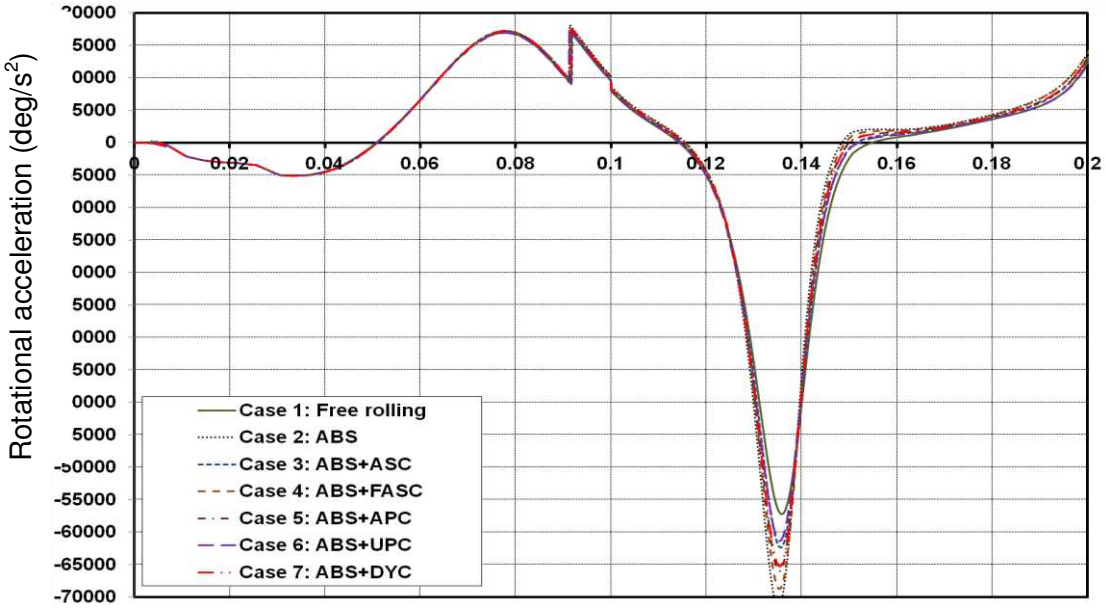

Figure 44: Rotational acceleration of the occupant's head about x axis (Offset frontal vehicle-to-vehicle impact), vehicle (b)

List of Tables

Table 1: The values of the different parameters, which are used in the simulations

Parameter	m	I_{yy}	I_{xx}	I_{zz}	I_{bzz}	$k_{SfR} = k_{SfL}$
Value	1200 kg	1490 $kg.m^2$	350 $kg.m^2$	1750 $kg.m^2$	40 $kg.m^2$	18.25 kN/m

Parameter	$k_{SrR} = k_{SrL}$	$c_{fR} = c_{fL}$	$c_{rR} = c_{rL}$	l_f	l_r	h	l_a
Value	13.75 kN/m	1100 N.s/m	900 N.s/m	1.185 m	1.58 m	0.452 m	1.2 m

Parameter	l_b	$b_i = b_o$
Value	0.85 m	0.8 m

Table 2: The values of the different parameters, which are used in the simulations

Parameter	m_1	m_2	m_3	l_2	l_3	L_1	L_2	L_3

Value	26.68 kg	46.06 kg	5.52 kg	0.427 m	0.24 m	0.3 m	2.3 m	0.65 m

Parameter	L_4	L_5	L_6	L_7	L_8	L_9	β	ζ
Value	0.3 m	0.35 m	0.45 m	0.55 m	0.97 m	1.1 m	30 deg	15 deg

Parameter	α	γ	ε_1	ε_2	ρ_1	ρ_2	k_{12}
Value	23 deg	30 deg	15 deg	15 deg	35 deg	43 deg	380 Nm/rad

Parameter	k_{23}	k_1	k_2	k_3	k_4	k_5	k_6
Value	200 Nm/rad	58860 N/m	39240 N/m	2500 N/m	2500 N/m	2500 N/m	2500 N/m

Parameter	c_1, c_2, c_3, c_4, c_5, c_6	d_{s1}, d_{s2}	d_{s3}, d_{s4}	d_{s5}	d_{s6}
Value	20% of the critical damping	0 m	0.05 m	0 m	0.05 m